The effect of upstream turbulence on a tip-vortex.

by

Prasath Krishnaswamy Varadharajan

to obtain the degree of Master of Science
at the Delft University of Technology,
to be defended publicly on December 6, 2019 at 10:00 AM.

Student number:	4620496	
P&E report number:	3014	
Project duration:	September 13, 2018 – December 6, 2019	
Thesis committee:	Dr. ir. G.E. Elsinga.	TU Delft, supervisor
	Ir. S. Nanda.	TU Delft, daily supervisor
	Prof. dr. ir. J. Westerweel.	TU Delft
	Dr. ir. I. Akkerman.	TU Delft

An electronic version of this thesis is available at `http://repository.tudelft.nl/`.

TU Delft

Acknowledgement

I would like to use this space to thank the people who helped me during the course of my masters education.

Pursuing masters in such an elite university is still a dream for so many people from my country. For me, this was possible because of my father, **K.Varadharajan** and my mother **Radha Varadharajan**. Thank you Appa and Amma, I could not have imagined this without you. I am forever grateful to both of you. I would also like to extend my gratitude to my brother, **Siddharth**.

I would like to thank **Dr.ir. Gerrit.E.Elsinga** for providing me with an opportunity to work under his guidance. Thank you for never saying no whenever I knocked your door for doubts. Your tips during the course of the thesis and support especially during the measurement campaign are greatly appreciated. I am very proud of the knowledge transfer and to have worked under your guidance.

I thank **Prof.dr.ir. Jerry Westerweel** and **Dr.ir. Ido Akkerman** for agreeing to be a part of my thesis committee.

Many thanks to **ir. Swaraj Nanda** for introducing me to this project. Your timely reality checks are hugely appreciated. I am also grateful to you for sharing with me the vortex detection code which helped immensely during the post-processing phase.

I would not have had a successful measurement campaign without the help from **Edwin Overmars**. I can't thank you enough for helping me with the measurement campaign and teaching me the nuances in conducting a good quality experiment. Thank you for being extremely approachable.

I would also like to thank **Jasper** and **Jan** of the Aero-Hydro lab for their timely help during my experimental campaign.

The 2.5 months of experimental campaign in the cavitation tunnel facility was possible with lot of support from **Peter Poot**. Thanks for helping me with the manufacturing of the grids and the frame in short notice. Your presence in the cavitation tunnel in the events of minor hiccups helped me to prevent it from becoming a major one.

Special thanks to **Drs. Evert Vixseboxse** for the moral support during extremely tough times of 2017. Thank you Evert ! I couldn't have imagined continuing my studies at TU Delft without your support.

Special thanks goes to my friend **Sudarshan** for the times we spent during the course of my masters program. I would also like to extend my gratitude to my batchmates **Akshar, Anshul, Nitish, Srinivasan, Vishal, Vignesh and Vivek** for making the study periods a memorable one. Lots of thanks to **Shravan, Udhav, Kalpit, Arjun** and **Anand** for providing an enjoyable company during the days at Aero-Hydro lab.

Prasath Krishnaswamy Varadharajan
Delft , November 2019

Abstract

A tip-vortex in the wake of a finite length lift generating surface has a low pressure region near the axis of the tip-vortex. This low pressure region can trigger tip-vortex cavitation especially in ship propellers which has adverse effects by causing vibration and underwater noise production. One way of minimising the tip-vortex cavitation is by reducing the propeller blade loading but at a cost of lower operating efficiency of the propeller. An alternative passive approach, to delay the onset of cavitation, by increasing the minimum pressure in the core of the tip-vortex through modification of the tangential velocity profile of the tip-vortex is investigated in this thesis.

In this thesis, the effect of upstream turbulence on the peak tangential velocity of the tip-vortex from a NACA 66_2-415 hydrofoil is investigated through stereo-Particle Image Velocimetry measurements. The turbulence is produced by a passive grid placed in the upstream of the hydrofoil. The tangential velocity profile at three different turbulent intensities were compared with measurements from a baseline no grid case that had nearly uniform and steady inflow to the hydrofoil.

The tangential velocity profile of the vortex exhibits a reduction in the average peak tangential velocity under the influence of the grid generated turbulence compared to the no grid case. The measurements taken at two downstream locations, 0.5 and 1.3 chord length downstream from tip of the hydrofoil, showed that a significant reduction in the magnitude of the average peak tangential velocity of the tip-vortex is observed only at the latter position. Also, on examining the axial velocity profiles, a significant reduction in the magnitude of the average peak axial velocity in the core of the tip-vortex was observed under the influence of grid generated turbulence.

An apparent effect of the upstream turbulence on the tangential velocity of the tip-vortex is seen to appear only when sufficient time is given for a secondary vortex structure, from the upstream turbulence, to form around and be intensified by the primary tip-vortex ([49],[21]). At 1.3 chord length downstream from the tip of the hydrofoil, the reduction in the magnitude of the peak tangential velocity is accompanied by increase core radius of the tip-vortex.

Contents

List of Figures

List of Tables

1 Introduction

This chapter begins with a brief introduction to the phenomenon of cavitation, tip-vorex cavitation and their adverse effects presented in section 1.1. Section 1.2 describes the motivation of the current study. The chapter ends with a summary of the structure of the report.

1.1. Cavitation and its impact on maritime industry

Cavitation is a rapid phase change process turning a liquid to its vapour. This process is dominantly observed in water which leads to boiling of water at a considerably lower temperature than commonly observed boiling temperature ($100°C$) of water. The change of phase is largely assisted by reduction in the local static pressure (hydrodynamic cavitation) of the water in contrast to application of heat. This phase change process occurs when the local static pressure of the water in the flow field equals the vapour pressure of the water (p_v) at that given temperature. A cavitation process can be broadly divided into three categories - bubble, sheet and vortex cavitation. These categories are so named that it relates to the dominant structures observed in the flow field during the phase change. Major effects of cavitation include erosion of material and noise generation due to the implosion of the cavity. Figure 1.1 shows different types of cavitation occuring in a marine propeller.

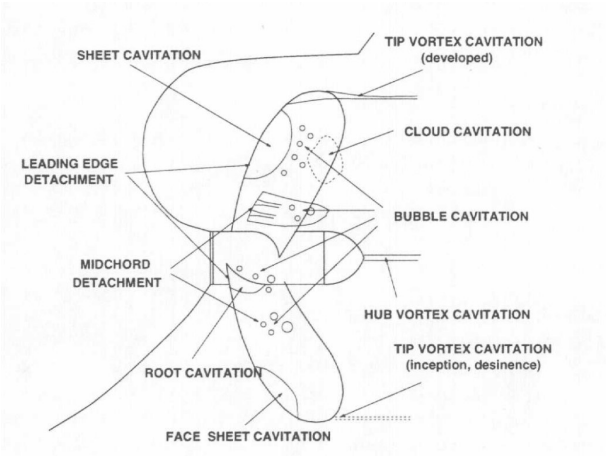

Figure 1.1: Different types of cavitation occurring over a marine propeller[1].

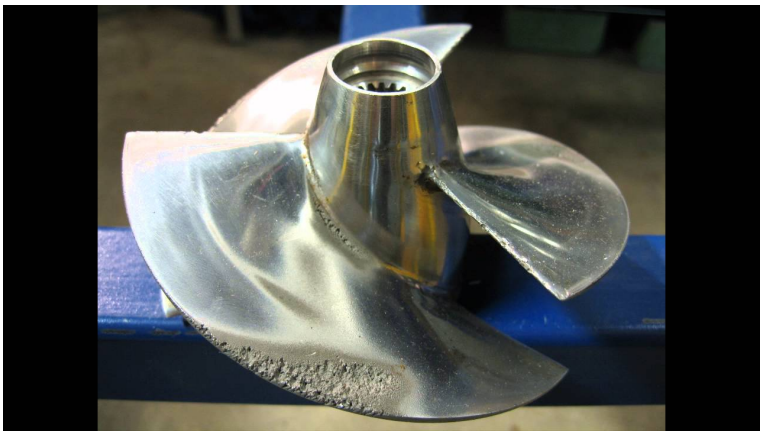

Figure 1.2: Photograph of a propeller showing the erosion of material on surface[2].

Figure 1.2 shows one of the adverse effects of cavitation- material erosion caused by implosion of cavitaties. Cavitation in ships predominantly occurs in the propeller region. As can seen from figure 1.1, various types of cavitation occurs in a marine propeller. In this thesis an approach, elaborated in section 2.4, to delay the occurence of tip-vortex cavitation is focused.

1.1.1. Tip-vortex Cavitation

Tip-vortex cavitation is majorly observed in a finite length lift generating surfaces such as hydrofoils and propellers. The trailing axial vortex from the tip of an hydrofoil (refer figure 1.3) has a low pressure region in its vortex core, owing to solid-body rotational flow, compared to its far field (ambient) pressure. When the pressure inside core goes below the vapour pressure of the water at that given temperature it results in a columnar cavity encompassing the tip-vortex. A typical isolated tip-vortex cavity from an hydrofoil is shown in figure 1.4

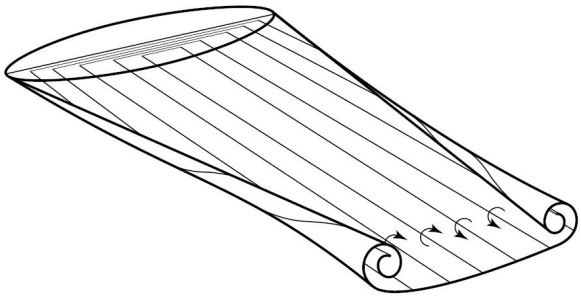

Figure 1.3: Schematic showing the tip-vortex formation along with roll-up process. [6].

Although, a mere reduction in static pressure to vapour pressure of the water is inadequate for cavity formation. Inception of cavitation also strongly depend on availability of nuclei and dynamics associated to nucleation [3]. Inception related studies from the perspective of nuclei and nucleation is not pursued in this thesis. The reader can refer to work by Rood[34] for an elborate discussion on inception dynamics. In this thesis, as will

be elaborated in section 2.4, minimum pressure in the core of a non-cavitating tip-vortex is investigated, indirectly, through peak tangential velocity.

Figure 1.4: Photograph of an isolated cavitating tip-vortex behind the hydrofoil. Flow direction is from left to right. [4].

1.2. Motivation

Understanding and the impact of the tip-vortex cavitation is of great concern for the maritime industry. It predominantly affects the performance of propeller reducing the thrust produced from the propeller and erosion of its material. Researchers constantly try to understand the mechanism behind the noise generated by the tip-vortex cavitation [5] given the noise signature it leaves behind. This is especially of great importance to the military application.

Noise generated from cavitation also has significant effects on the marine biology as the communication between animals under the water is affected by noise from the cavitation, among other noises from the ship vessels [39]. Studies by Prins et al. [33] specifically mentions the interference of cavitation into marine animals' communication through cavitation noise produced from propellers. One of the prime objectives of their study was to take measures to design the propellers that are free from cavitation noise.

The above mentioned studies form only a small part of large researches conducted in field of cavitation and tip-vortex cavitation. Given the adverse effects like underwater noise generation, material erosion and decrease in performance, measures are taken by the industry and researchers to understand (tip-vortex)cavitation and suppress its negative effects. Thus it is worthwile to study the tip-vortex phenomena in the context of current research interests and feasibility.

1.3. Structure of the report

This report is organised in the following manner

- Chapter 2 contains relavant background theory, literature consulted for the current thesis and the research objective and questions of the current study.
- Chapter 3 elaborates on the philosophy adopted in designing the grid. The subsequent section in the chapter contains the details of experimental setup used in this

thesis and the choice of measurement parameters for PIV experiments. A preview to the results presented is schematically depicted at the end of the chapter.

- Chapter 4 presents the results in two parts. First part presents the results from planar PIV measurements that characterize the inflow to the hydrofoil. Second part presents the average velocity profile measured around the tip-vortex downstream of the hydrofoil at two downstream positions.

- Chapter 5 summarises and dicusses the two main conclusions of this study. The thesis ends with few recommendations for carrying forward this study from the findings of this thesis.

2

Background theory and literature review

This chapter gives an overview of the relevant fundamental concepts and the literature considered in this thesis. Sections 2.1 and 2.2 briefly touch upon the important concepts of vortical flows and grid turbulence, pertaining to this thesis, respectively. Section 2.3 elaborates on literature considered for the current thesis followed by aim and research questions of this thesis in sections 2.4. The chapter ends with the scope of this thesis in section 2.5

2.1. Vortical flows

A vortical flow is a commonly observed flow pattern in everyday life. A most common instance of such a flow can be witnessed while draining the water from an household kitchen sink or a bathtub. Most striking observation in such flows is the circular or nearly circular flow pattern of the fluid. By definition vorticity, $\vec{\omega}$, is a vector field which is equal to curl of the velocity vector.

$$\vec{\omega} = \vec{\nabla} \times \vec{u} \tag{2.1}$$

2.1.1. Velocity distribution of standard vortical flows

Vortical flows are broadly classified into two categories namely irrotational vortex (free vortex flow) and solid body rotation (forced vortex flow). For a simplified case in absence of radial and axial flow, the distribution of tangential velocity of a solid-body rotational flow in polar coordinate system is given by

$$u_\theta(r) = \Omega r \tag{2.2}$$

where Ω is the plane normal angular velocity.
For an irrotational vortex, the tangential velocity distribution is given by

$$u_\theta(r) = \frac{\Gamma}{2\pi r} \tag{2.3}$$

where Γ, a scalar quanitity, is called the circulation of the vortex. Γ is also representative of the strength of the vortex.

In an idealistic irrotational vortex, the vorticity in the flow field is zero everywhere except at the centre of the vortex where it is infinite. On contrary, the vorticity of the solid-body rotational flow is constant throughout the flow field and is equal to twice the angular velocity, Ω.

2.1.2. Static pressure distribution in a typical vortical flow

A simplified radial equilibrium flow which is a) steady, b) axisymmetric, c)has zero radial velocity and d) the axial and tangential component of velocity and pressure vary only radially, is representative of the flow over a lifting surface, like hydrofoil or airfoil.

For such a case, the only non-trivial component of momentum equation is the radial component expressing the balance between centripetal force and radial pressure gradient.

$$\frac{\partial p}{\partial r} = \rho \frac{u_\theta^2}{r} \tag{2.4}$$

The tip-vortex generated in downstream of the lifting surface has solid body core and irrotational an field outside the core. A Rankine vortex model for such flows predicts the tangential velocity distribution as

$$u_\theta(r) = \Omega r \quad ; 0 \leq r \leq r_c \tag{2.5}$$

$$u_\theta(r) = \frac{\Omega {r_c}^2}{r} \quad ; r_c < r < \infty \tag{2.6}$$

where Ω is the angular velocity and r_c is the vortex core radius defining the boundary between the solid-body core and the irrotational region.

From the radial momentum equation the distribution of pressure can be obtained for simple cases of such radial equilibrium flows. The pressure distribution is given by

$$\frac{p(r) - p(0)}{\rho} = \frac{\Omega^2 r^2}{2} \quad ; 0 \leq r \leq r_c \tag{2.7}$$

$$\frac{p(r) - p(r_c)}{\rho} = \frac{\Omega^2 {r_c}^4}{2r^2} \quad ; r_c < r < \infty \tag{2.8}$$

where $p(r)$ is the static pressure at a radial position r from the axis of vortex and $p(0)$ is pressure in the axis of the vortex. In real tip vortices behind an hydrofoil, core of the vortex has a solid-body rotational flow where the axis line pressure, $p(0)$ is lowest. If and when $p(0)$ goes below the vapour pressure (p_v) of the water, at that given temperature, cavitation is prone to occur forming water vapour.

From equation 2.7 and 2.8, after re-arranging,

$$p(0) = p(\infty) - \rho \Omega^2 {r_c}^2 \tag{2.9}$$

we see that the minumum pressure in the core, $p(0)$ increases with decrease in Ω at a constant $p(\infty)$, which, in many situations, is constant far field ambient pressure. In this thesis, it is aimed to passively decrease Ω that can help to maintain the minimum pressure, $p(0)$, higher than p_v. Through this passive control, cavitation inception can be delayed or avoided. An elaborate discussion on the research objective is given in section 2.4

2.2. Grid Turbulence:

The term turbulence is hard to be defined exactly. Although, necessary features for a flow to be turbulent can be easily observed and described. Important features of turbulent flows are diffusive behaviour, randomness and presence of vortical structures or eddies. Turbulent flows are also highly dissipative in nature which means a constant inflow of energy is required for the turbulence to sustain. A typical turbulent flow in the downstream of a grid is shown in figure 2.1. Eddies of different sizes can be observed which is an important characteristic of a turbulent flow.

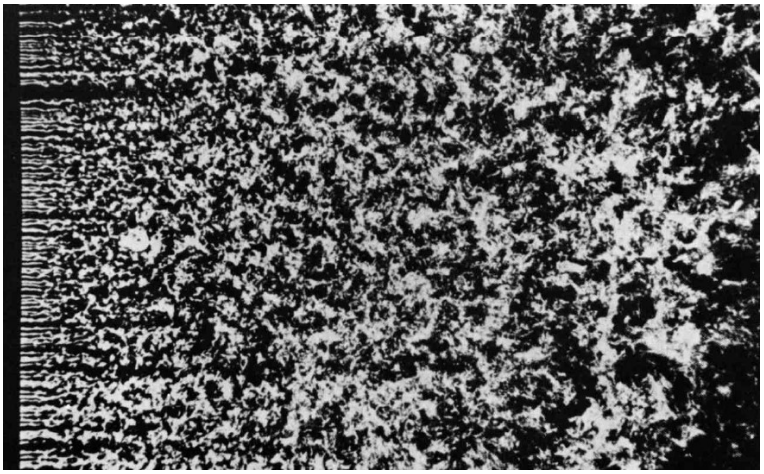

Figure 2.1: Flow visualization of grid generated turbulence. Image reproduced from Album of fluid motion by Milton van Dyke([37]).

Flow through a grid at large Reynolds number, based on the mesh width (M) of the grid (figure 2.2), for instance 10,000 ([27]) generates turbulence.

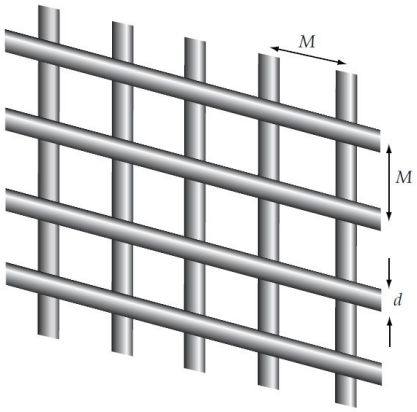

Figure 2.2: Schematic showing the geometrical parameters of a turbulence generating grid. Image reproduced from [32].

The turbulence behind a grid can be characterised using various quantities like turbulent intensity (T.I.), turbulent kinetic energy (TKE, k), dissipation rate (ϵ) and integral length scales (I.L.S., Λ).

Using Reynolds decomposition, the velocity vector in a turbulent flow can be decomposed into two parts, mean and fluctuation. The decomposition is given as

$$u_i = \overline{u_i} + u_i' \tag{2.10}$$

where $\overline{u}_i$ is the mean of instantaneous velocity (u) and u' is the fluctuating part. The overbar represents the averaging operation. To quantify the relative turbulence level in the flow, the parameter turbulent intensity ($T.I.$) is commonly used. It is defined as

$$T.I._i = \frac{u_{irms}}{U} \tag{2.11}$$

where u_{irms} is the root-mean-square of fluctuations of velocity vector component and U is the characteristic velocity of the mean flow.

Turbulent kinetic energy (k) is representative of the energy contained by the large eddies. These large eddies transfer the kinetic energy across smaller eddies where it is finally dissipated by action of viscosity. An expression for turbulent kinetic energy, summed over three coordinate directions, is given by

$$k = \frac{1}{2}\overline{u_i'^2} \tag{2.12}$$

2.2.1. Flow behind a grid

Numerous studies have been conducted since the 1930s ([36], [11], [46], [27], [17]) on grid generated turbulence as it considered one of the basic forms of turbulence ([32]). The region downstream of the grid is classified into 3 sub-regions ([27]). First is the developing region nearest to the grid where the rod wakes are merging, the flow is inhomogeneous and anisotropic, and consequently there is production of turbulent kinetic energy. This is followed by the second region where the flow is nearly homogeneous, and locally isotropic and where there is appreciable energy transfer from large eddies down to smaller eddies. It is in this region that the form of the power-law decay mentioned in equation 2.14 is applicable. The third region or final period of decay, where viscous effects act directly on the large energy containing scales is farthest downstream from the grid.

As turbulence is dissipative in nature and thus in the absence of mean shear ($= \partial\overline{u_i}/\partial x_j$), like in the flow behind a grid, the velocity fluctuations decay along downstream distance. For a homogeneous decaying isotropic turbulent flow, evolution of TKE is given [32] by

$$\frac{Dk}{Dt} = -\epsilon \tag{2.13}$$

where D/Dt is the material derivative and ϵ is the dissipation term defined by $\nu\overline{(\partial u_i'/\partial x_j)^2}$.

The decay of the turbulent intensity along the downstream distance can be expressed as ([23])

$$\left(\frac{u_{rms}}{U_0}\right)^2 = A\left[\frac{X - X_o}{M}\right]^{-n} \tag{2.14}$$

where X is the downstream location behind the grid from the virtual origin, X_0 , U_0 is the mean inlet velocity to the grid, n is the decay exponent and A is the grid dependent coefficient. The decay exponent (n) is not universally constant ([25], [17]). Initial conditions

of the flow and the dimensions of the grid play an important role in deciding the value of n. A sample power law decay of the turbulent intensity from the work of Kurian & Fransson [23] is shown in figure 2.3.

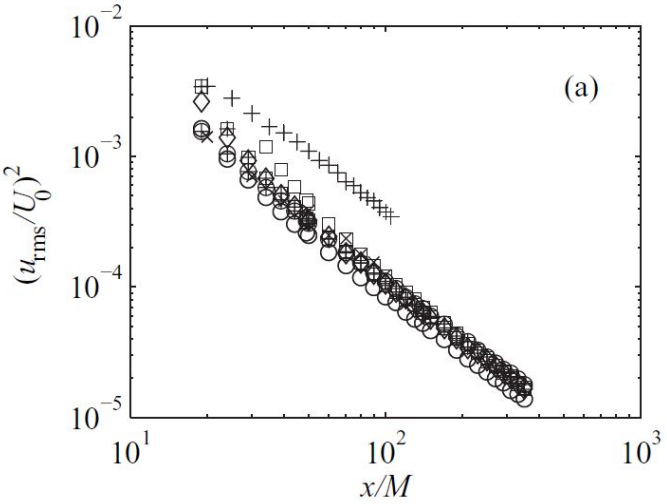

Figure 2.3: Log-log plot showing the decay of turbulent intensity ($T.I.$) along the downstream of the grid. Each symbol represent a specific grid. Y axis- square of the magnitude of the turbulent intensity. X axis - downstream distance normalised with mesh width, M. Image reproduced from([23]).

In turbulent flows, size of the large scale structures eddies scale with the characteristic length scale of the flow. In grid turbulence, the characteristic length is the mesh width (M) of the grid [36]. The large scale structures thus scale with the mesh width (M) of the grid. Integral length scale, a statistical quantity, is a measure of size of large scale structures. In grid turbulence the integral length scale increases along the downstream distance. This does not mean the large eddies grows in size downstream, it is rather that smaller and less energetic eddies decay quickly leaving behind large eddies (refer figure 2.1). An estimate for evolution of large scales can be derived from the fundamentals of turbulence theories. The disspiation rate scales as $\epsilon \sim \frac{\overline{u_i'^3}}{\mathscr{L}}$ where $\mathscr{L}$ is the size of the large eddies. Now, considering $k = \overline{u_i'^2}$, an estimate of size of large eddies is given as $\mathscr{L} \sim \frac{k^{3/2}}{\epsilon}$. The mentioned scaling gives only an approximate estimate of the size of the eddies. More accurate and realistic values of the integral length scale (stream-wise) at a point x, y in the flow field is computed from the longitudinal auto correlation function ($\rho_{11}(r, s = 0)$) given by

$$\rho_{11}(r, s = 0) = \frac{R_{11}(r, s = 0)}{\overline{u'(x, y)^2}} = \frac{\overline{u'(x, y)u'(x + r, y)}}{\overline{u'(x, y)^2}} \tag{2.15}$$

where r represents the physical distance between the two points at x, y and $x + r, y$, in flow field. The overbar in the expression is the averaging operator (here, time averaged). In equation 2.15, s =0 represents $1D$ auto-correlation. When s $\neq$ 0, it means a $2D$ auto-correlation. To give a physical understanding, $\rho_{11}(r, s = 0)$ represents the level of correlation between the fluctuations at two points in stream-wise direction separated by distance r. The dimensionless quantity ρ_{11} takes highest value of 1 at the reference point x, y and

decreases while moving away from it eventually dropping to 0. The stream-wise integral length scale (Λ_{11}) is given by

$$\Lambda_{11} = \int_0^\infty \rho_{11}(r, s=0)\,dr = \int_0^\infty \frac{\overline{u'(x,y)\,u_i'(x+r,y)}}{\overline{u'(x,y)^2}}\,dr \tag{2.16}$$

2.3. Literature Review

2.3.1. Effects of upstream turbulence on tip-vortex

Tip-vortex or trailing vortex, as they are called in aircraft fraternity, is a well explored phenomenon. The need for a detailed exploration in the topic, since 1970s, was motivated by the fact that aircrafts leave behind a strong pair of tip-vortices from their wings during landing and take-off whose strength can cause structural damage to a follower aircraft. From a safety perspective, it was important for the air traffic control fraternity to understand the strength and life time of such vortices to efficiently and safely space the take off and landing intervals of the departing and arriving aircrafts ([35]). Spalart [35] provided a detailed review on trailing vortices and put forth observations collectively from flight tests and simulations indicating rapid decay of tip-vortices under ambient free-stream turbulence. In the same timeline, studies, predominantly flow visualizations and hot-wire velocimetry measurements, were already being done on the effects of free-stream[1] turbulence on the tip-vortex downstream of airfoil.

One of the early studies was carried out by Bandyopadhyay et al.[10] to quantify the effects of free stream turbulence on isolated tip-vortex behind a NACA 0012 cross-section airfoil. The flow visualization and hot-wire annemometry measurements were carried out to study the effect of different free-stream turbulent intensities, generated using grids, on the velocity profiles and the Reynolds stresses in the trailing vortex at a downstream position 40 chord length from the tip. It was observed that the magnitude of the peak tangential velocity decreased with increase in (from 0.03% to around 4.85% near the leading edge of the airfoil) turbulent intensity. A clear trend in the reduction of peak tangential velocity with increase in the core radius of the tip-vortex. Reynolds number of the experiments is not precisely mentioned in the work. Investigations on partial relaminarization of turbulence in the core of the vortex were also carried out in the their work. The relaminarization in the core that resticts the tansport of momentum by turbulence away from vortex axis was attriubuted to the coriolis effect.

Although investigations by Sarpkaya [48] provided data from field flight tests on tangential velocity and circulation strength of trailing vortex from an aircraft, the data was limited to single test of different aircrafts. Also, the turbulent intenisity was only estimated indirectly through non-dimensional dissipation rate (ϵ^*). The absolute tangential velocity data from the work could not be used for understanding general behaviour.

Numerical simulation (DNS) by Melander & Hussain [49] to investigate coupling of coherent structure and fine-scale turbulence showed interesting organisation of background

[1] The terminology free-stream and upstream turbulence means one and the same. The usage depends on the field of application.

fine-scale turbulence around a coherent tip-vortex. At a circulation Reynolds number,Re_Γ(= Γ/ν) of= 665.2, it was seen that after a sufficient development of the flow, the background fine-scale incoherent turbulent sturctures were made coherent by the primary tip-vortex. The vorticity of the fine-scale turbulence, azimuthally alinged around the tip-vortex (refer figure2.4a), were intensified due to stretching provided by the primary tip-vortex. The magnitude of vorticity of these secondary structures were found to be appreciable only around primary tip-vortex compared to far-field magnitude. Apart from the organization of the structures around the tip-vortex, time dependent energy spectrum analysis highlighted the possible cascade of energy from small wave-number coherent tip-vortex to large wavenumber fine-scale turbulence around it. The work highlighted the effects of different initial free-stream turbulent intensities. A low intensity did not affect the primary vortex significantly while a high level of turbulence lead to complete breakdown of the primary vortex.

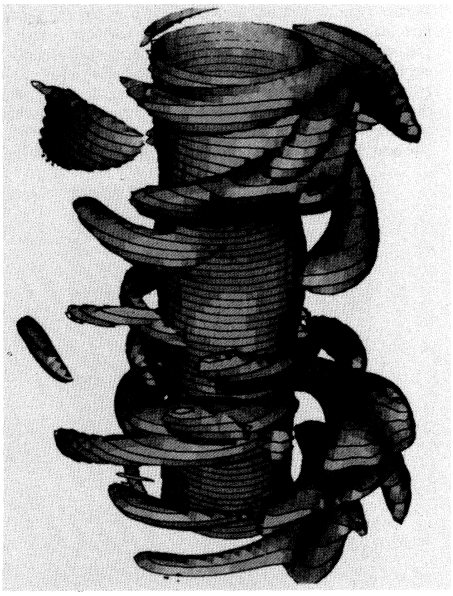

(a) Isovorticity surface produced from the simulations, at Re_Γ = 665.2, depicting the coherent tip-vortex surrounded by secondary vortical structures [49].

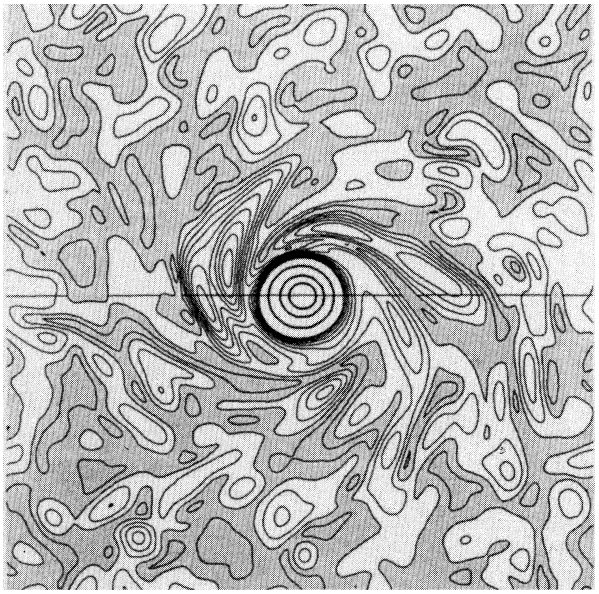

(b) Vorticity norm,at Re_Γ = 665.2, in cross-sectional plane perpendicular to tip-vortex axis. Lowest value shaded in grey[49].

Figure 2.4: Results from simulation showing (a) the azimuthally aligned secondary structures around the tip vortex and (b) the contour of vorticity in the plane perpendicular to the vortex axis.

Bailey et al.[9] conducted hot-wire measurements around a tip-vortex in the downstream of a NACA 0012 cross-section airfoil. The inflow to the airfoil was analysed at two different upstream turbulent intensity, 2.5% and 5% at the leading edge, and a baseline uniform flow at 0.4%. The upstream turbulence was generated using grids of mesh width 25.4 mm (T.I.=2.5%) and 50.8 mm (T.I.=5%). At a Reynolds number of 2.4×10^5, based on chord length of airfoil (C), near field measurements at locations of 1.75, 5.75 and 9.75 chord lengths downstream from the leading edge resulted in tangential velocity profiles of the tip-vortex at the mentioned upstream conditions. The relative unceratainty in the normalized

average tangential velocity ($\overline{u}_\theta/U_0$, U_0 being mean freestream velocity) was mentioned to be around 0.5%.

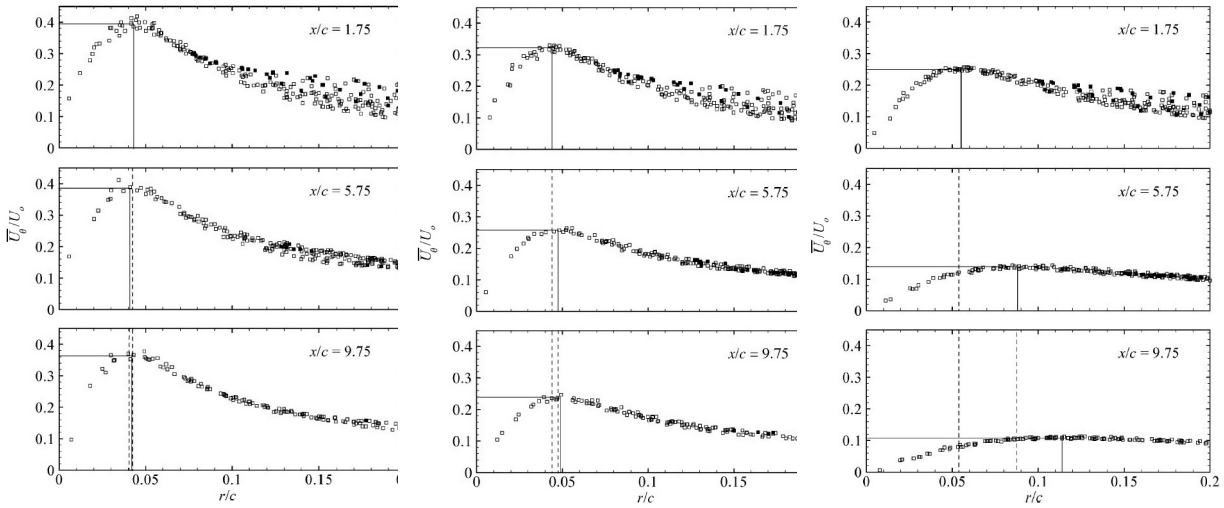

(a) No grid case. **(b)** Small grid case. **(c)** Large grid case

Figure 2.5: Radial variation of average tangential velocity($\overline{u}_\theta/U_0$) of tip-vortex. (a)-(c) show the velocity profiles at turbulent intensity of 0.04%, 2.5% and 5% respectively. Image reproduced from [9].

Average tangential velocity profiles from [9], figures 2.5a-2.5c, show the effect of upstream turbulent intensity at three different downstream locations. The reduction in the average peak tangential velocity is apparent with increase in upstream turbulent intensity while the effect is magnified at a larger downstream location than nearer to the airfoil. The reduction in the average peak tangential velocity was accompanied by increase in the radius of the core of the tip-vortex.

Beninati & Marshall [14] conducted velocimetry measurements using hot-wire annemometry technique. Apart from average tangential velocity, they measured and presented the radial profiles of turbulent kinetic energy (TKE) and reynolds stresses in the core of the tip-vortex, behind a NACA 0012 airfoil, under turbulent upstream conditions at a chord Reynolds number of 97500. Grid of mesh width 0.5 cm generating turbulence were placed 30 cm upstream of the airfoil. The core of the vortex was observed to contain high levels of TKE for the test case with grid compared to a baseline no grid case. The profiles of the streamwise turbulent intensity was found to be highest at a point close to the centre of the vortex and not at the centre of the vortex axis. This could possibly be due to existence of the secondary structures around the tip-vortex mentioned by [49].

LES study by Holzapfel et al.[21] on effect of ambient turbulence on tip-vortex shows presence of organized motions around the tip-vortex like mentioned in [49]. These authors also elaborates on the mechanism which causes a distinct decay of the tip-vortex under the influence of high free-stream turbulence level. The free-stream incoherent turbulent vortices are stretched, tilted and organised around the primary tip-vortex on the expense of the energy from the primary tip-vortex. This is happens in the initial stages after the formation of tip-vortex. Farther downstream, these secondary vortices in the expense of its

energy causes rapid decay of the primary tip-vortex.

One of the recent experimental study on vortex-turbulence interaction was done by Ghimire & Bailey[18]. Stereo-PIV technique was employed in this study to investigate vortex decay at downstream position of 0.96 and 6.56 chord lengths, from the trailing edge, under two different turbulent intensities and a baseline uniform inflow. An increase in the decay rate of the vortex circulation under turbulent free-stream conditions was observed with no increase in the rate of increase of the core radius. This can be inferred as loss of angular momentum under the influence of free-stream turbulence. At the location 0.96 chord length downstream, the average peak tangential velocity does not reduce significantly for different upstream turbulence intensities. The growth in core radius and reduction in magnitude of peak tangential velocity was found to be very apparent at the downstream position of 6.96 chord lengths from the trailing edge.

Ghimire & Bailey [43], using stereo-PIV technique, assessed the decay characteristics of the tip-vortex under turbulent free-stream conditions. The experiments were carried out in a tow tank facility at Reynolds number, based on chord length of NACA 0012 airfoil, of 17000. The rapid decay of the tip-vortex observed in their previous work ([18]) was attributed to the presence organised secondary vortical structures around the tip-vortex. Reason for such a decay was seen to arise from distortion of the vortex core by the surrounding vortical structures which itself was characterized by ejection of swirling fluid from the core. Intensity of this ejection events increased with increase in free-stream turbulent intensity. The rapid decay was found to happen only after 5 chord lengths downstream of the tip-vortex.

2.3.2. Grid generated turbulence

In previous section, the literature cited contained works on effects of free-stream turbulence on tip-vortex characteristics. In these studies, predominantly, higher levels of free-stream turbulence was achieved through grid generated turbulence owing to the simplicity in the operation of these (passive) grids. Given the nature of the available test facility for this thesis, it was decided to proceed with similar approach of using grids to generate turbulence in the upstream of the hydrofoil. The grid design methodology considered for the current thesis is elaborated in chapter 3.

Grids, in form of screens, are used in most flow apparatuses to improve the flow uniformity. On contrary, flow through these grids at large Reynolds number, based on the mesh width (M) of grid, generates turbulence [23]. Thus before desiging the grid, it was important to ensure we fall in the second category, i.e, to generate higher turbulent intensity, more than an amount when a grid is not used, that must reach the tip-vortex from the hydrofoil. The level of turbulent intensity is decided by geometric parameters like grid porosity,β and mesh width,M. The porosity of the grid is representative of the open area to the total area of the grid.

Various studies on grid turbulence were carried out to understand physics of turbulent intensity decay along the downstream distance (Taylor [36], Mohamed & LaRue[27],George [17],Batchelor & Townsend[12],Batchelor & Townsend[11]). Important take aways from these studies are mentioned as follows:

- There exists a separate decay physics at developing region in the immediate vicinty

of the grid compared to developed regions downstream of the grid. Choice of geometrical parameters decide the development length[36].

- In the developed region, the decay of turbulent intensity follows a power-law given by

$$\left(\frac{u_{rms}}{U_0}\right)^2 = A\left(\frac{X - X_0}{M}\right)^{-n} \tag{2.17}$$

  In many past studies, if not all, power-law region started at least after 10 mesh widths downstream of the grid. This region is then followed by final decay period.

- Decay rate exponent (n) and coefficient (A) is dependent on initial conditions of the flow. Scatter in the values of n is evident from the data presented in the above mentioned studies. This implies a straight forward prediction of decay to achieve certain level of turbulent intensity at required downstream position is not advisable.

- Laws & Livesey [26] proposed an expression for the decay of the turbulent intensity, that is given by

$$\frac{U_0^2}{\overline{u'^2}} = b\frac{X - X_0}{M * K} \tag{2.18}$$

  where K is an indirect measure of grid porosity. From this, it can be seen that at a constant porosity, thus constant K, increase in mesh width M leads to increase in turbulent intensity at a given downstream position X. Here, b is considered to be equivalent of A from equation 2.17. Tennekes & Lumley [50] mentions that at limiting condition of perfect isotropic turbulence, n attains a value of 1. Thus comparing the above mentioned two equations, although they are not straightforwardly the same equations, the background physics is preserved.

Studies by Lavoie et al. ([25] [24]) mentions the effect of the initial conditions on the structures of the turbulence downstream. Initial conditions here refer to the geometrical parameters (β, M, d) of the grids. Grids with square and circular rods of same mesh width were studied. Test cases with different porosity was also studied. It was inferred that varying grid porosity affected only the large scale structures of the the flow. In their study, grid with lower porosity(β), of 0.56 compared to 0.65, generated higher turbulent intensity.

In the context of the scatter in decay exponents observed in the literature ([17], [27]) and presence of initial condition dependence ([25],[24]), it was thus decided to choose a mesh width to scale with required length scales to be generated while maintaining a grid porosity (β) of 0.56. A detailed discussion on the philosophy adopted in designing the grids for this thesis is given in chapter 3.

2.4. Objective of the research

In this section, findings from the literature reviewed is assimilated and a brief explanation is given on how the objective and research questions of the thesis were formulated.

As seen from equation 2.7, the radial pressure difference in the core of the vortex is given by

$$\frac{p(r)-p(0)}{\rho} = \frac{\Omega^2 r^2}{2} \quad ;0 \leq r \leq r_c$$

The minimum pressure in the core of the vortex, $p(0)$ increase with decrease in the angular velocity Ω . This radial pressure gradient in a the core of tip vortex is derivded from the simplified radial momentum equation that is given by

$$\frac{1}{\rho}\frac{\partial p}{\partial r} = \frac{u_\theta^2}{r} \tag{2.19}$$

It is seen that the peak tangential velocity dictates the radial pressure gradient in the core of the typical tip-vortices. Indeed, if the core of the vortex behaves like a solid body rotational flow then the pressure increases radially outward. The studies mentioned in section 2.3.1 show us evidences of reduction in peak tangential velocity ([10], [9], [18], [43]) of a tip-vortex under turbulent upstream conditions. This is seen as an opportunity to alter the radial pressure gradient indirectly, thus the minimum pressure in the core of the tip-vortex. This may eventually avoid or delay the onset of tip-vortex cavitation.

With such a possibility available, it is worthwhile to investigate the effects of free-stream turbulence on tip-vortex specfically focusing on the magnitude of the average tangential velocity. Also, many of the experimental studies in the literature were carried out using hot-wire annemometry technique. Given the phenomenon of vortex centre wandering [44], which increases with increase in free-stream turbulence, a whole field measurement technique is preferred over single point measurement technique for more accurate detection of vortex centre. This serves as an important motivation to employ Particle Image Velocimetry technique to carry out this investigation.

Bailey et al.[44] proposes a scaling for amplitude of vortex wandering. During the process of vortex wandering, caused by momentum transfer between turbulent eddies and the vortex, there should exist a specific time for the interaction. This time over which the momentum transfer happens is governed by the rotation rate of the vortex. In the context of momentum transfer, which causes the decay of the tip-vortex, it was motivating to carry out atleast brief analysis to quantify the vortex wandering in the current thesis. The main objective of this thesis can thus be summarised as

" To study the effect of upstream turbulence on an isolated tip vortex downstream of a NACA 66_2-415 hydrofoil using stereo-Particle Image Velocimetry technique"

The following research questions were formulated to achieve the objective of the study.

- How is the average peak tangential velocity of the tip-vortex altered under turbulent inflow condition compared to a uniform inflow condition ?
- How does the turbulent inflow condition affect the wandering of vortex centre ?

To answer these questions, it is aimed to carry out the experiments under two circumstances - in the absence and the presence of the upstream grid generated turbulence at three different turbulent intensities. The measurements are to be carried out at two different locations downstream of the hydrofoil. The turbulent inflow conditions due grid generated turbulence at the upstream of vortex are also to be characterized by finding the integral length scale and turbulent intensity using planar PIV measurements.

2.5. Scope of the current thesis

- Interest of present study is to see how the turbulence affects the peak tangential velocity, thereby indirectly affecting minimum pressure in the core of the vortex as minimum pressure in the core is also a driving factor in the inception of cavitation. With the interest in the velocity profile, all the velocimetry measurements are carried out for non-cavitating tip-vortex only. No measurements were conducted for a cavitating case. Also, cavitation inception from the perspective of nucleation dynamics is not of interest in the current study.

- The turbulent inflow conditions generated by the grids are assumed to be isotropic in nature. Isotropic relations are to be employed in calculating statistical quantities as and when needed.

3

Methodology and experiments

This chapter starts with methodology adopted in designing the grids in section 3.1. Section 3.2 briefly describes the test facility used in this thesis. Section 3.3 details on how the parameters for planar and stereo- PIV experiments were chosen. Finally, in section 3.4 a preview to how the results are presented is given.

3.1. Grid design methodology

The design phase of the grid is critical as it majorly decides the nature of the flow in its downstream. As mentioned in chapter 2, very fine mesh generally removes free stream turbulence while coarse mesh generates turbulence [26]. The coarseness is defined by the parameter porosity (β) which represents the ratio of open to total area of the grid. In current study it is intended to generate nearly isotropic turbulence using passive grids which will serve as upstream condition for the hydrofoil. The choice of parameters in designing the turbulence generating grids is stated below.

3.1.1. Choice of grid parameters

Geometry of a grid is described by 3 important parameters, namely mesh width (M), grid porosity (β), wire diameter (d). Figure 3.1 shows the schematic of a bi-planar grid. The mesh width, M is the distance between centres of 2 adjacent parallel rods and wire diameter, d is the diameter of the cylindrical rod.

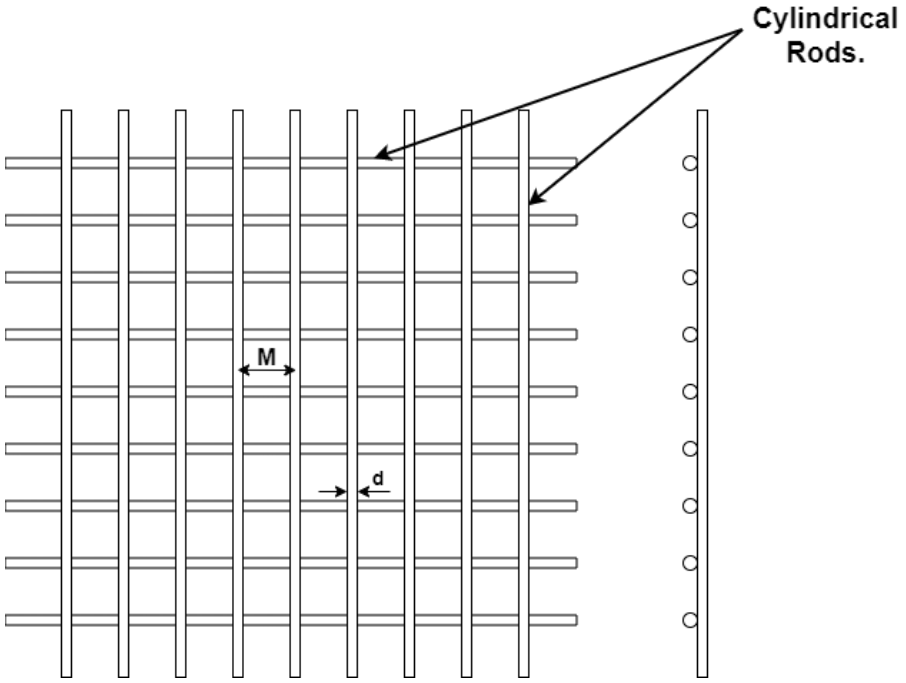

Figure 3.1: Front view (left) and side view (right) schematic of a grid indicating the mesh width (M) and wire diameter (d).

Mentioned below is the guideline that was followed while assigning values for the parameters mentioned above.

- Kurian & Fransson[23] mentions the grid porosity (β) defined by

$$\beta = \left(1 - \frac{d}{M}\right)^2 \tag{3.1}$$

  must be maintained above 0.55. Maintaining a lower value than prescribed would lead to merging of jet from adjacent mesh holes.

- Taylor [36] mentions that for wire a diameter $1/4^{th}$ of the mesh width, the wind shadow of the grid disappears within few mesh widths as opposed to extending over $30M$ when not. A developed turbulent flow is preferred over a developing flow(wind shadow) which can be closely approximated to isotropic turbulence.

- The integral length scale of grid turbulence scales with the mesh width, M of the grid.

3.1.2. Design Philosophy:

The aim of the thesis, in short, is to impose turbulent inflow condition in the upstream of the tip-vortex and study the vortex characteristics. In the initial phase of this thesis it was also planned to carry out shadowgraphy measurements on a cavitating tip-vortex. Keeping this in mind, the grids were designed to excite the cavitating tip-vortex at resonance frequency[30] equivalent length scales generated from the grid.

But later during the experimental campaign, it was seen that the cavitation tunnel could not reach desired velocity to generate a cavitating tip-vortex. Thus all the experiments were conducted on non-cavitating tip-vortex with these same grids.

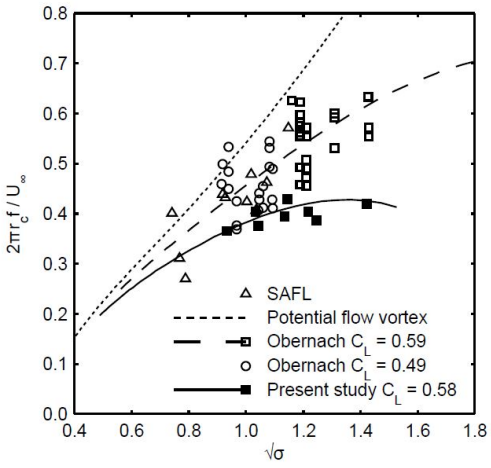

(a) Variation of dimensionless frequency as a fucntion of $\sqrt{\sigma}$. 'Present study' mentioned in the plot means the work by Pennings [29].

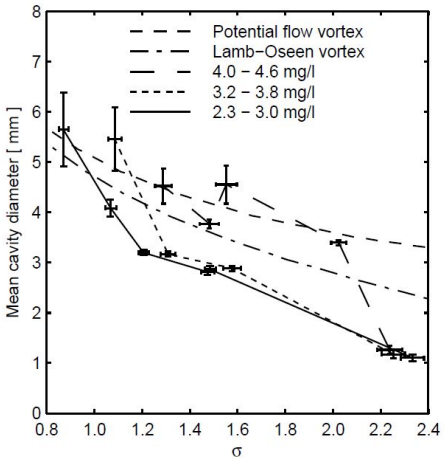

(b) Variation of mean cavity diameter as a function of cavitation number.

Figure 3.2: Data from [29] that was used in finding the resonance frequency equivalent length scales.

An estimate of resonance frequency equivalent length scales were obtained from the study of [29]. Figure 3.2a gives a relation between $\sqrt{\sigma}$, where σ is the cavitation number, and the dimensionless frequency is as shown below

$$\frac{2\pi r_c f}{U_\infty} = F(\sqrt{\sigma}) \tag{3.2}$$

where r_c is the tip-vortex cavity radius at the corresponding cavitation number (σ) and f is the resonance frequency of the waves on the interface of the cavitating tip-vortex. A length scale, U_∞ / f, can be obtained if the cavity radius is known at the corresponding cavitation number (σ). This data was also available(figure 3.2b) from the study of [29].

From figure 3.2b, cavity radius is found at cavitation numbers pertaining to the test case where oxygen content is between 2.3-3.0 mg/l. The estimated radius were 2.84mm, 2.05mm, 1.61mm, 1.42mm, 0.56mm. For a parametric study, 3 cases were considered to further estimate an equivalent length scale. The equivalent length scales thus estimated, using equation 3.2, were 31.34mm , 25.72mm and 21.96mm.

These obtained values were proposed as the mesh width, M of the grid. It was decided to use cylindrical rods([25]), hence the wire diameters were $1/4^{th}$ of these estimated mesh widths. This gives 7.83mm, 6.43mm and 5.49mm as diameters of the cylidrical rods. Considering the feasibility of manufacturing and availability of the stainless steel rods the wire diameters were fixed to 5mm, 6mm and 8mm which gives the mesh width of 20mm, 24mm and 32mm. Table 3.1 summarises the geometric details of the the manufactured grids.

Grid	Type	Mesh width, M (mm)	Wire diameter, d (mm)	Porosity,β
Grid1	Cylindrical rod, Bi-planar	20	5	0.56
Grid2	Cylindrical rod, Bi-planar	24	6	0.56
Grid3	Cylindrical rod, Bi-planar	32	8	0.56

Table 3.1: Nomenclature and geometrical parameters of the grids.

Figure 3.3 gives the dimensional details of one of the grid and frame. Figure 3.4a and 3.4b show the CAD models of the manufactured grid along with the frame. The frame which houses the grid is inserted between the test section and contraction part. The grid-frame setup was designed to facilitate quick change of grids without removing the test section.

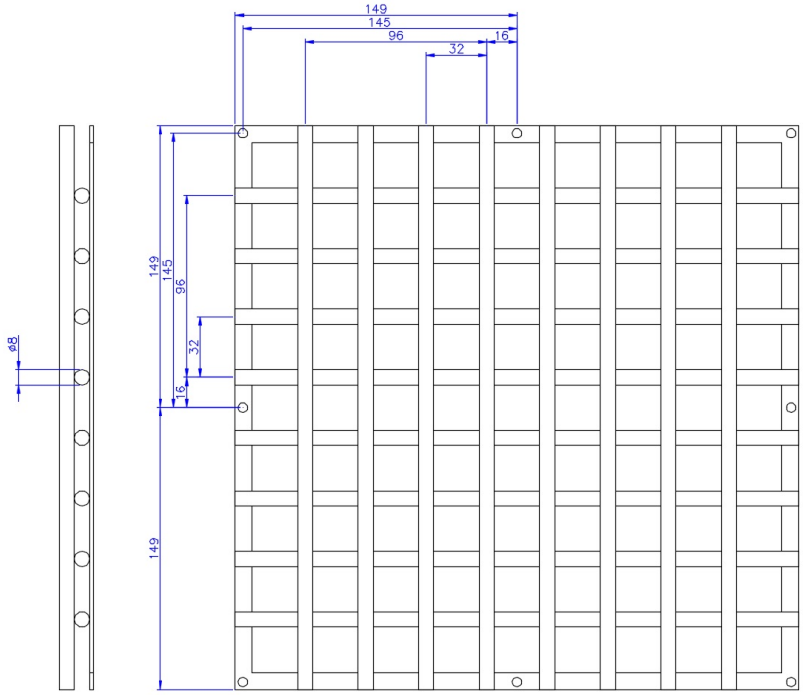

Figure 3.3: Sample drawing showing the dimensions of grid (Grid3) and the frame.

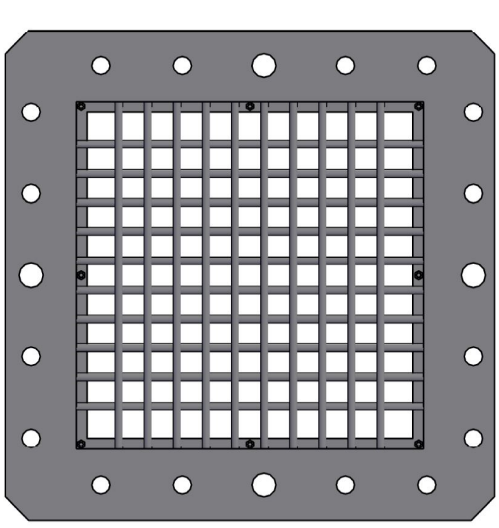

(a) Front view of the grid along with the frame.

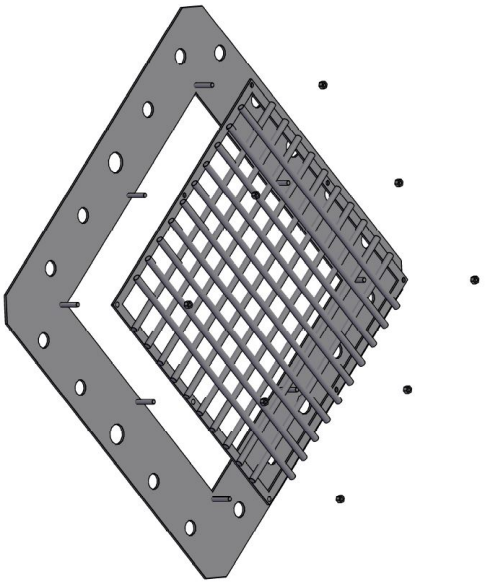

(b) Exploded view of the grid and the frame.

Figure 3.4: Sample CAD models of the grid along with the frame.

3.2. Test Facility: TU Delft Cavitation tunnel

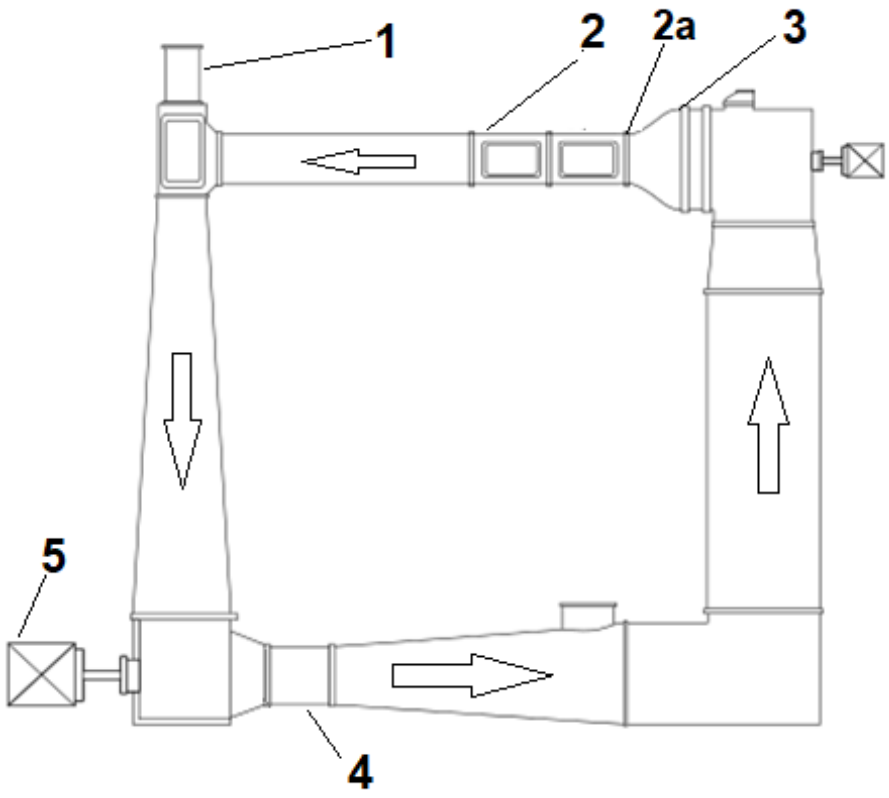

Figure 3.5: Schematic of cavitation tunnel test facility. 1) De-aeration chamber, 2) Test section, 2a) Location of grid with frame, 3) Contraction, 4) Impeller casing, 5) Electrical motor drive. The flow direction is as indicated by the arrows.

The experiments were performed in the cavitation tunnel facility at the ship hydromechanics department of TU Delft. Figure 3.5 shows the schematic of the cavitation tunnel depicting various parts of the tunnel. The manufactured grids along with the frame were placed between test section (2) and the contraction (3) (2a in figure 3.5). The de-aeration chamber along with vaccum pump system was used to create a safe operating condition of the tunnel. The free stream tunnel velocity is determined from the pressure drop over the contraction measured with a differential pressure sensor (Validyne®DP 15), that was calibrated before the start of the campaign. The required inlet velocity was set through a LabVIEW©program.

3.2.1. Description of the test Section

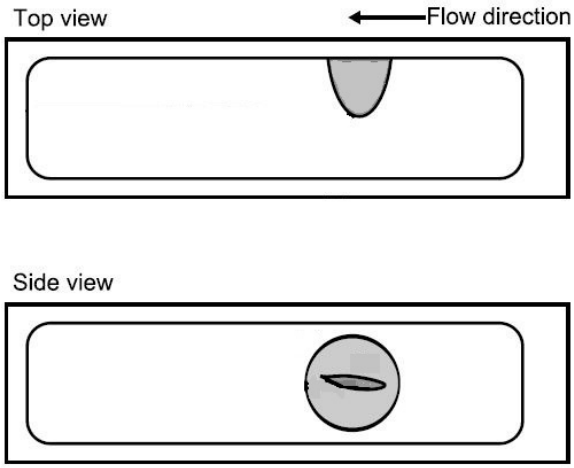

Figure 3.6: Schematic of test section. Figure not to scale. Image taken and edited from [29]

The cross-section of the test section was $0.30 \times 0.30 m^2$ at the inlet and $0.30 \times 0.32 m^2$ at the outlet [29]. The hydrofoil has an elliptic planform and a NACA $66_2 - 415$ cross section with root chord length, $C = 0.1256 m$. The hydrofoil has a half span of 0.15 m. Thus, the tip is positioned in the centre (span-wise) of the test section. The hydrofoil is mounted on the side window of the test section on a disk containing a six-component force/torque sensor (ATI SI-330-30).

3.3. Design of experiments

As the inflow to the hydrofoil was made turbulent using passive grids in the upstream, it is important to know the turbulent intensity and the integral length scales generated by the grids. The experimental campaign required the first part, to characterize the the inflow to the hydrofoil. Tip-vortex velocimetry measurements was the subsequent campaign. The following sub sections details on the choice of experimental parameters for the experimental campaigns.

3.3.1. Inflow characterization - Planar PIV measurements

The planar PIV measurements are carried out for three grids (Grid1, Grid2, Grid3) and one baseline condition (NoGrid) with no grid inserted. Measurements for each grid is carried out at three set inlet velocity (U_{0set}) conditions viz; 1m/s, 2m/s, 3m/s.

The two main quantities used in the current study for characterization of the inflow, and the grids, are turbulent intensity and integral length scales in the downstream of the grid. Employing planar-PIV technique for estimating these quantities is ideal as PIV gives whole-field instantaneous velocity of the flow region under study. These instantaneous velocity fields can then be utilised to evaluate the turbulent intensity and the integral length scale generated by the grid.

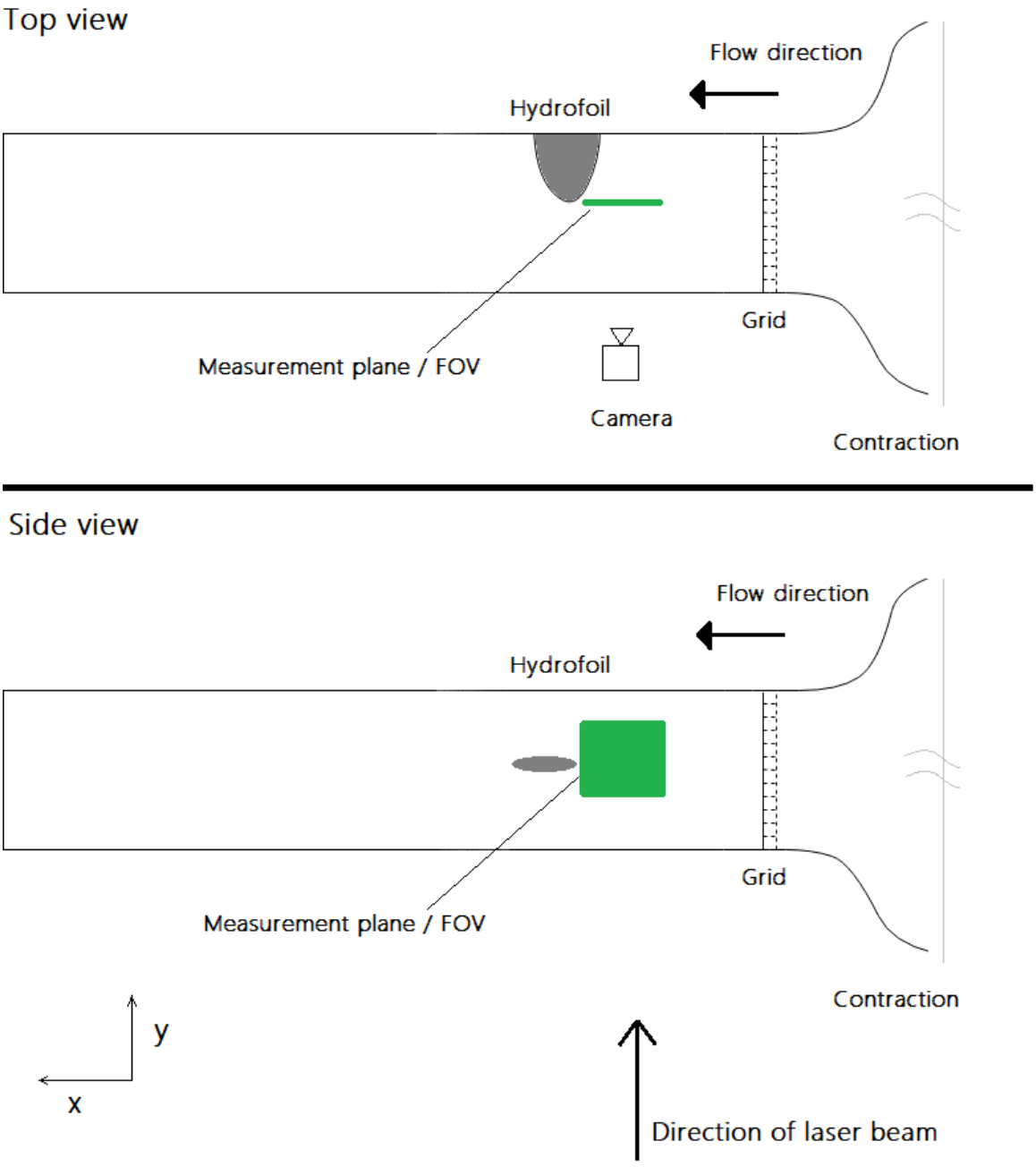

Figure 3.7: Schematic of Planar-PIV measurement setup. Figure not to scale.

Planar PIV measurements provide in-plane velocity data of the flow region under study [7]. For current planar PIV measurements, a measurement plane which is parallel to mean flow and perpendicular to the tip of hydrofoil was chosen(refer figure 3.7 & 3.8). The plane was positioned at the centre of test section, aligned with the tip of the hydrofoil.

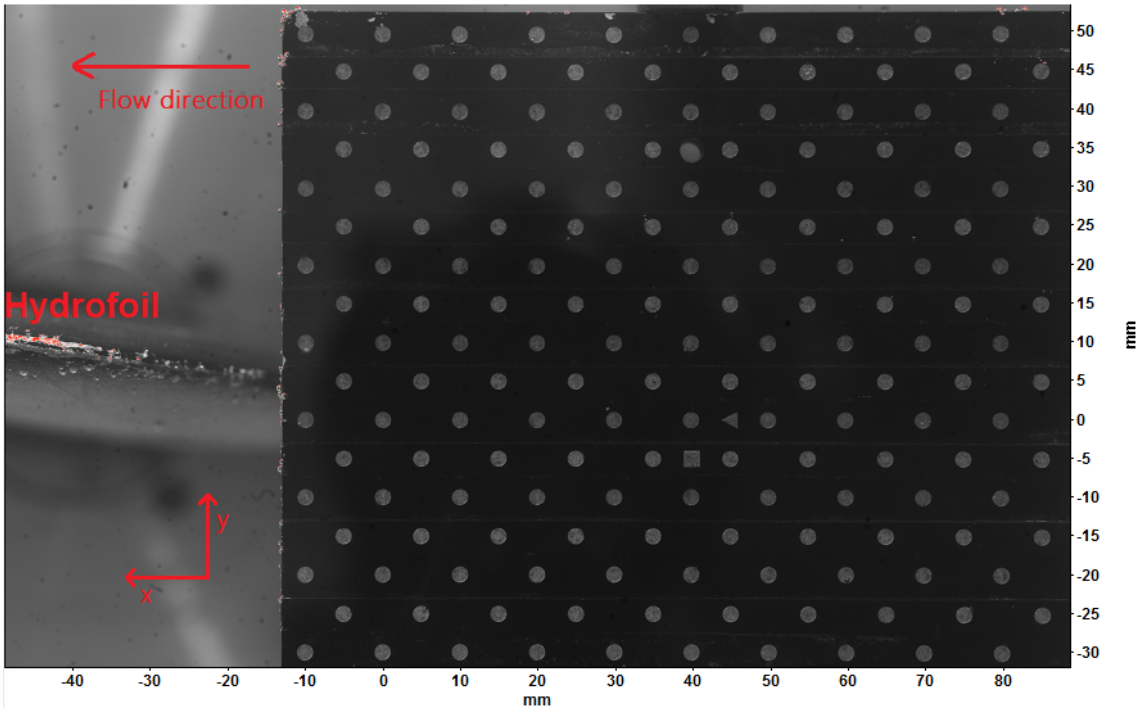

Figure 3.8: Image showing the span of FOV in mm. Tip of the hydrofoil (left) along with calibration target is also seen in the image.

Selection of measurement plane:

The region of study (field of view, FOV) where velocity data was gathered spanned approximately 13.5cm and 9cm in x and y-direction respectively. The location of the centre of the FOV was approximately 6.5cm upstream of tip of the hydrofoil and at the same vertical location of the tip (refer figure 3.8). The FOV was chosen such that it spans approximately a chord length upstream of the hydrofoil.The choice of position of FOV was an optimal choice between the fact to not encounter the developing turbulence from the grid (as much as possible) and to have enough spatial extent for estimation of integral length scales and the decay of turbulent intensity. It was also ensured to be not too close to the hydrofoil to avoid reflections caused by laser sheet hitting the hydrofoil.

Measurement parameters:

The flow was seeded with tracer particles(sphericel®110P8) of 12μm mean diameter whose density was 1.10 $\pm$ 0.05 g/cc. The scale factor for current set of experiments were 35 pixels/mm, where each pixel is 7.4μm. This gives a magnification of around 0.26. The FOV was illuminated using double-pulse Nd:YAG laser of wavelength 532nm. The particle images were acquired with high resolution (4872x3248 pixels) LaVision ImagerProLX low speed camera at acquisition rate of 0.7Hz for 2000 image pairs. The slow acquisition rate ensured temporally uncorrelated image image samples. A 105mm Micro-Nikkor lens was used with $f^{\#}$ set at 5.6. The particle image diameter was observed to be 2-4 pixels, on an average. The choice of pulsation separation time (Δt) is one of the most important parameter to be decided and set during a PIV experiment. As a standard practice [7], Δt is set such that

particle image displacement corresponds to $1/4^{th}$ of the size of desired interrogation window. For example, 8 pixels considering a 32x32 window size. In pixel units, for such particle image displacements the turbulent fluctuations, represented as standard deviation (u_{irms}) of the velocity, was found to be in the sub-pixel range. For example, even at a maximum of 10% turbulent intensity, an 8 pixel particle image displacement would result in 0.8 pixels of u_{rms}. Thus a much larger particle displacements, 30pixels on an average in mean flow direction (here x direction) was adopted. Such method was also adopted by Poelma et al. (2006)[31] in their grid turbulence study. For the current set of measurements, a quick Δt sweep study was carried out to check for the change in standard deviation of u while incresing Δt. A final Δt was fixed (refer table 3.2) considering the 30pixel displacement criterion, quality of correlation and percentage of 1^{st} choice vectors provided by DaVis (>93%). A multi-pass, 3 passes, decreasing interrogation window size approach was adopted for calculation of vectors. A 48×48 interrogation window at the final pass with 50% overlap was used for calculation of vectors.

Set Inlet Velocity (U_{0set}) [m/s]	Δt [μ sec]			
	Grid3	Grid2	Grid1	No Grid
3	260	275	285	265
2	390	400	400	400
1	850	800	800	800

Table 3.2: Laser pulse separation time (Δt) for each of the test cases in μsec.

3.3.2. Tip vortex velocimetry - Stereo-PIV measurements

Stereo-PIV technique is employed to obtain the velocity field around the tip-vortex. Stereo-PIV measurement provides in-plane (here w & v) and out of plane (here u) velocity components on a 2D measurement plane. Figure 3.9 shows a schematic of the measurement setup for the stereo-PIV campaign.

Measurements were taken at each of the set inlet velocity (viz 1m/s, 2m/s, 3m/s) using each of the manufactured grid (Grid1, Grid2, Gird3) and at baseline condition (No-Grid). The angle of attack was set at 9°, pointing downwards, for all of the cases. Two measurement planes were chosen downstream of the hydrofoil. With the tip of the hydrofoil taken as reference position, where $x/C = 0$, the two planes were located at $x/C = 0.5$ and $x/C = 1.3$. As an exception, the measurements on plane $x/C = 1.3$ were taken at only 2m/s for all the 3 grids and no grid condition.

Selection of measurement plane:

The highest peak tangential velocity of the tip vortex exists closer to hydrofoil. Along downstream of hydrofoil, the tip-vortex decays thereby also the peak tangential velocity. The peak tangential velocity determines the minimum pressure inside the tip-vortex core. Thus, in context of the research interest, it was useful to choose a downstream measurement plane close to the hydrofoil. Also, previous studies invariably carried out experiments at a location more than chord length downstream. It was not completely clear of what was happnening in the near field. Thus a near-field plane at the location $x/C = 0.5$ was chosen. A second measurement plane was chosen to use the data for mutual cross-verification of

results obtained from the two planes and compare with literature. As the laser optics were mounted on a precision traverse which had a working range from 0, fixed at $x/C = 0$, to 100mm, the location of second plane was limited to $1.3C$ from the tip of the hydrofoil.

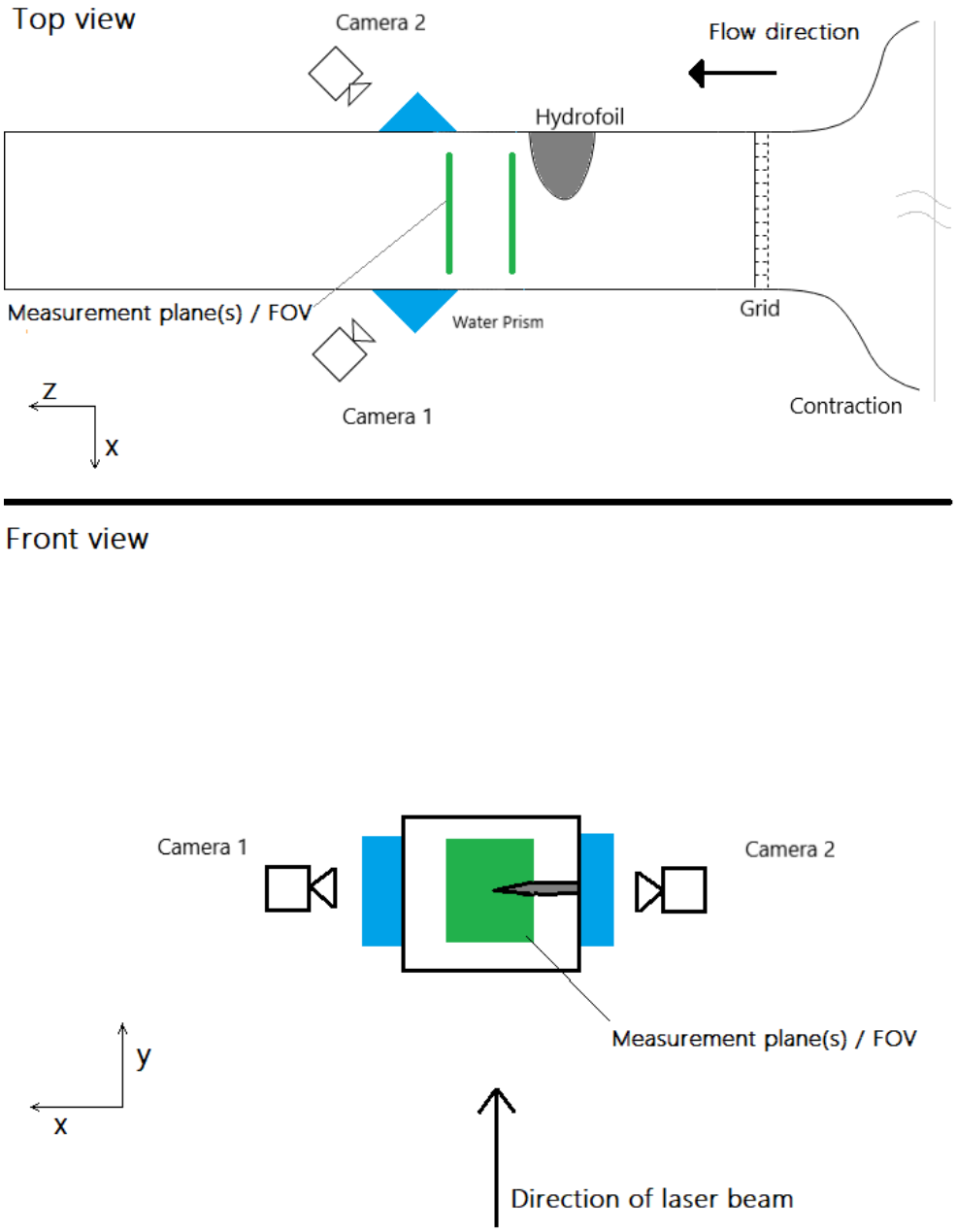

Figure 3.9: Schematic of Stereo-PIV measurement setup. Figure not to scale.

Measurement parameters:

The flow was seeded with tracer particles (sphericel ®110P8) of 12μm mean diameter whose density was 1.10 ± 0.05 g/cc. A double-pulse Nd:YAG laser with wavelength of 532nm was used as source for illuminating the FOV. Two ImagerPro LX cameras (4872×3248 pixels), attached with a scheimpflug adapters, were used to obtain particle images on the measurement planes. A total of 2000 image pairs were obtained at an acquisition rate of 0.7Hz. The FOV for first plane spanned approximately 8cm and 10cm (refer figure 3.10a). A 105 mm Micro-Nikkor lens was used with $f^{\#}$ set to 8. The particle image diameter was tried to be maintained between 2-4 pixels although deviations were observed away from the centre of FOV due to distortion effects while satisfying sheimpflug condition. The cameras were then re-adjusted to bring the (anticipated) vortex location close to centre of FOV. A final standard calibration was again performed after re-adjustments. A resolution of minimum of 30pixels/mm was achieved. The pulse separation time (Δt) was maintained such that the out of plane particle displacement was less than $1/4^{th}$ the thickness of the light sheet. A multi-pass, 3 passes, decreasing interrogation window size algorithm with 32×32 in the final pass was used to calculate vectors. An overlap of 75% was used as well. The motivation for oversampling was to ensure that the obtained vectors are able to capture the velocity profile around the vortex more smoothly compared to a 50% overlap usage.

For each dataset obtained, a self-calibration procedure [52] using the corresponding particle images (1000 images) was performed before calculating the vectors.

The same procedure was followed for acquiring and processing all the datasets in the plane $x/C = 1.3$. The dewarped FOV is shown in figure 3.10b

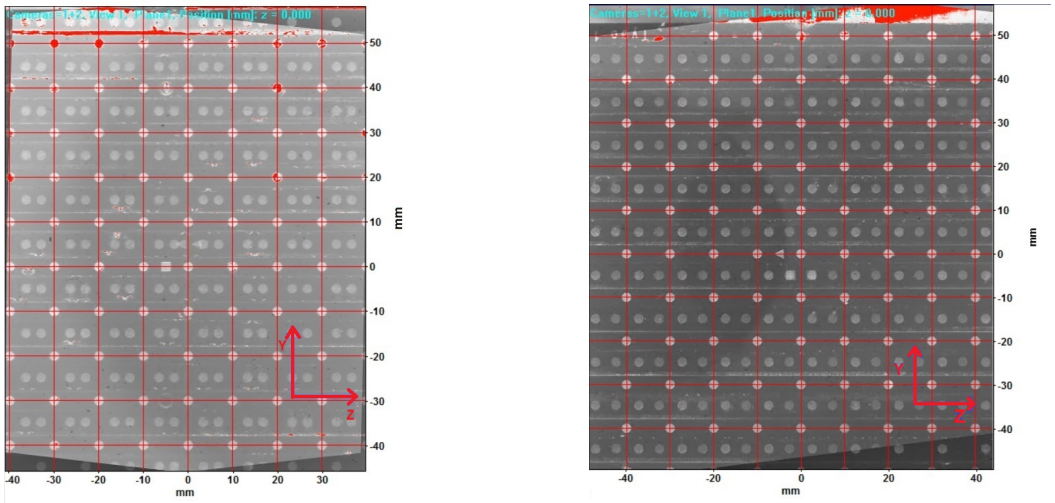

(a) FOV of the measurement plane at $x/C = 0.5$. **(b)** FOV of the measurement plane at $x/C = 1.3$

Figure 3.10: Dewarped images of the FOV pertaining to stereo-PIV measurements.

3.3.3. Vortex centre detection

The particle images were processed using DaVis 8.4 software to obtain instantaneous velocity vector fields around the tip-vortex. The first step towards the calulation of average velocity profile of the tip-vortex is to detect the centre of the tip-vortex. Two methods were initially considered to detect the centre, namely gradient and integral method (Graftieaux et al.[19]).

Gradient method:

In gradient method, the centre of vortex is located by finding location of peak axial vorticity (ω_x). The calculation of the axial vorticity utilizes the straight-forward relation given by

$$\omega_x = \frac{\partial w}{\partial y} - \frac{\partial v}{\partial z} \tag{3.3}$$

The location of the the peak vortex, found after smoothing operation (7×7 moving average), is then fixed as the vortex centre.

Integral method:

Graftieaux et al.[19] presented an algorithm where the centre of vortex is calculated using an integral quantity. The proposed integral quantity, Γ_1 ranges from 0 at far field to 1 at vortex centre. The quantity Γ_1 applicable on discrete PIV data is given by

$$\Gamma_1(P) = \frac{1}{N}\sum_S \frac{(PM \wedge U_M).z}{\|PM\|.\|U_M\|} = \frac{1}{N}\sum_S sin(\theta_M) \tag{3.4}$$

where P is a fixed point in measurement domain, S is a 2D area surrounding P, M is any point lying in S, z is the unit vector normal that measurement plane, U_M is the velocity vector at M, θ_M is the angle between the velocity vetor U_M and radius vector PM and N is the number of points (M) in S. Figure 3.11 is a schematic explaining the above mentioned quantities used in vortex detection.

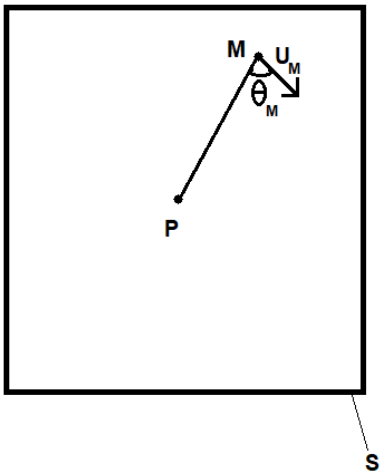

Figure 3.11: Schematic depicting the implementation of the integral method.

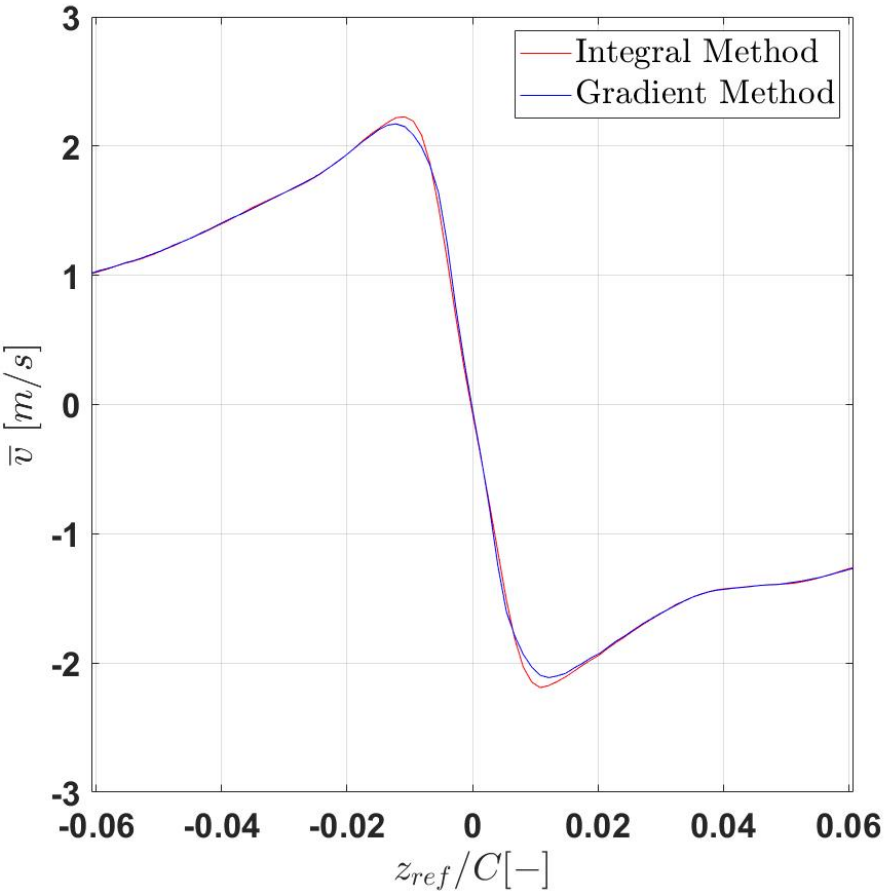

Figure 3.12: Average tangential velocity($\overline{v}$) profile obtained using gradient and integral method.

An example of the comparative study done between the two methods is shown in figure 3.12. It is evident from figure 3.12 that integral method captures the peak tangential velocity sharper than gradient method. The gradient method seems to provide a smeared out profile. The analysis was carried out for the case of Grid3 at 3m/s and 2m/s at $x/C = 0.5$. Subsequent to this analyis, it was decided to post-process the vector fields of all the test cases using integral method to obtain average velocity profiles of the tip-vortex.

3.4. Data processing and preview of results

3.4.1. Inflow characterization

The instantaneous velocity vector fields were obtained after processing the particle image pairs using DaVis 8.4 software. 2000 instantaneous velocity vector fields were obtained in the end which were then post processed using MATLAB©to obtain turbulence statistics. Three quantities namely, mean inlet velocity (U_0), turbulent intensity (T.I.) and integral length scales (Λ) are used to characterize the inflow conditions and the grid. A reference point is chosen in the upstream of the hydrofoil and all the parameters are calculated at this reference point.

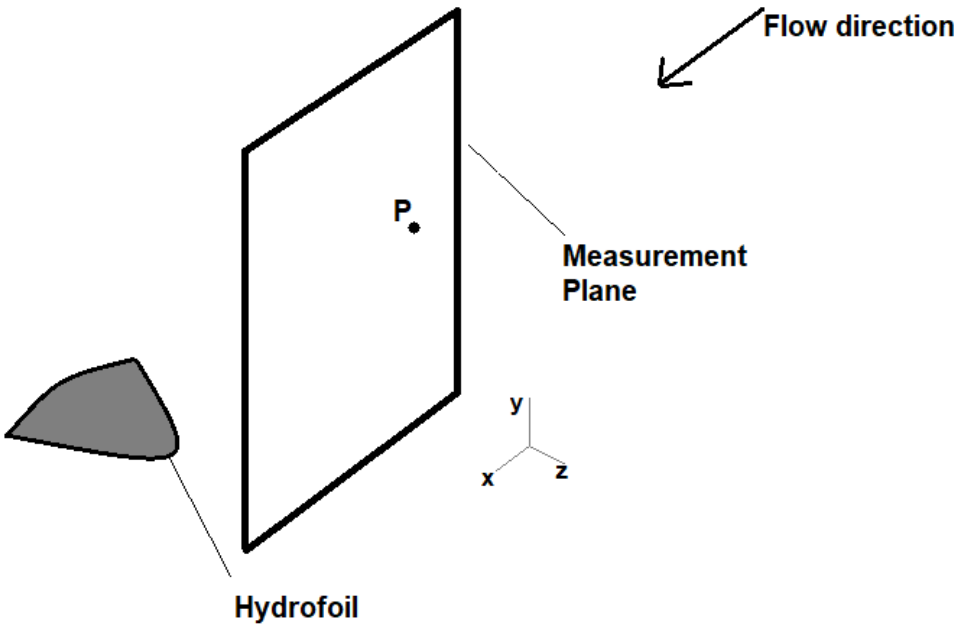

Figure 3.13: Schematic showing the plane $(x-y)$ in which turbulence statistical quantities are computed and presented. $P(x_0, y_0)$ is the reference point. u and v are the velocity components in x and y direction respectively.

The quantities to be presented in the results chapter are listed below.

- Mean inlet velocity (U_0) at the reference point.
- The turbulent intensity decay along the downstream direction (x), from the reference point in the upstream of the hydrofoil is presented. The downstream distance is normalized by chord length of the hydrofoil.
- Stream-wise integral length scales computed for each grid at the reference location.

3.4.2. Vortex characteristics

The velocity fields around the vortex were conditionally averaged, with respect to vortex centre, to obtain the time averaged tangential and axial velocity profiles. For all the 2000 time steps, the vortex centre is detected and fixed as origin ($x_{ref} = y_{ref} = z_{ref} = 0$). The vector fields were then averaged over 2000 time steps.

The average velocity components, namely, $\overline{v}$ along z at $y = y_{ref} = 0$ and $\overline{w}$ along y at $z = z_{ref} = 0$ represent the tangential velocities of the vortex. The average velocity component $\overline{u}$ along z at $y = y_{ref} = 0$ represents the axial velocity in the cartesian co-ordinate system.

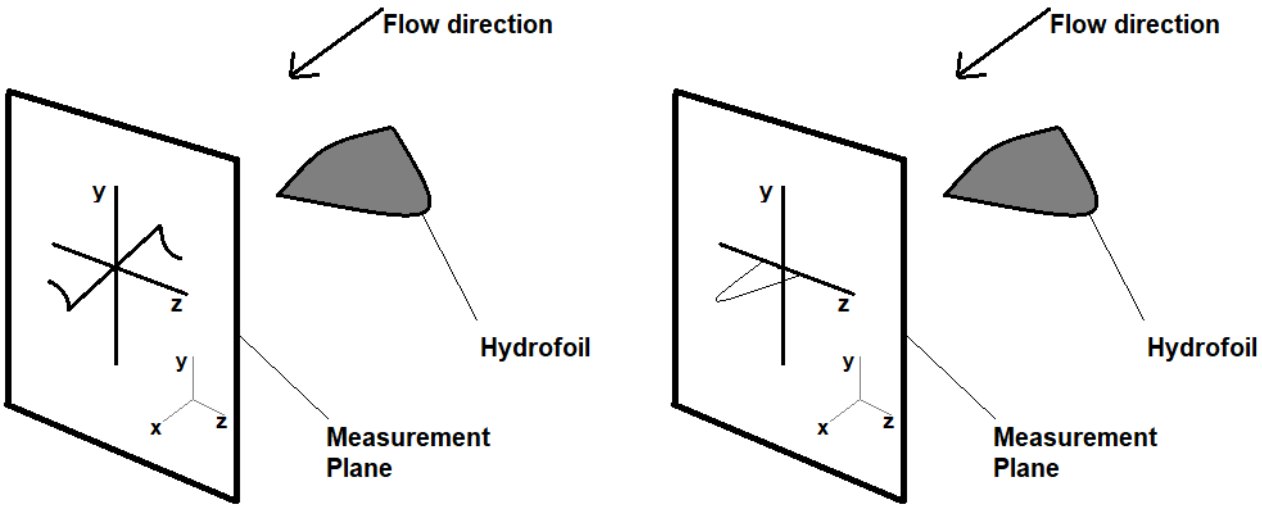

(a) Average tangential velocity ($\overline{w}$) along y.

(b) Average axial velocity ($\overline{u}$) along z

Figure 3.14: Schematic of later presented (section 4.2.1) velocity profiles with coordinate system. y and z are the inplane axis and x is the out of plane axis. u, v and w are the velocity components in x, y and z direction, respectively.

A list of results to be presented in section 4.2 is given below.

- The average tangential velocity profiles ($\overline{v}$ along z and $\overline{w}$ along y in the $y-z$ plane) and axial velocity ($\overline{u}$ along z in the $y-z$ plane) are presented. The velocity profiles are normalized with the corresponding mean inlet velocity (U_0) and chord length (C) of the hydrofoil in the abcissa. Similarly, profiles of root-mean-square(rms) of fluctuation of v and w velocity normalized with mean inlet velocity (U_0) and chord length (C) is presented.
- Probability density functions(PDF) of distance between mean and instantaneous vortex centre location normalized by chord length(C) is also presented. This PDF is quantitative measure of vortex wandering. The PDFs of both horizontal and vertical wandering of the vortex centre is presented.

4

Results and discussions

In this chapter, the results of planar-PIV and stereo-PIV measurements are presented. Firstly, results of planar-PIV measurements that characterizes the inflow is presented in section 4.1 followed by results of stereo-PIV measurements describing the vortex profiles and vortex centre wandering in section 4.2.

4.1. Inflow Characterization

The inflow condition at the upstream of hydrofoil is described using three quantities, namely, mean inlet velocity (U_0), turbulent intensity (T.I.) and stream-wise integral length scales (Λ_{11}). These quantities were calculated at a reference location (x_0, y_0) that is 12cm upstream of the hydrofoil and approximately at the same vertical position of the tip of the hydrofoil (for a quick and simple visualization refer figure 3.14a and 3.14b). The choice of reference point which is located close to a chord length (C) distance upstream is chosen to avoid possible upstream influence from the hydrofoil [20].

4.1.1. Mean Inlet velocity (U_0)

The value of set inlet velocity (U_{0set}) does not reflect on the actual mean inlet velocity (U_0) to the hydrofoil due to the cross-section change between the point where the U_{0set} is measured and the point where reference point is located. Thus, it is important to know the actual mean inflow velocity (U_0), at the reference point (x_0, y_0), upstream of the hydrofoil. To calculate the mean inlet velocity, the obtained instantaneous velocity fields are first time averaged over 2000 times steps and later spatially averaged about the reference point in vertical (here y-axis) direction. The spatial averaging was done over a span of 7.8 cm containing 116 vector values. Table 4.1 shows the obtained values of U_0 for each case.

Set Velocity,U_{0set}(m/s)	Actual inlet velocity, U_0 (m/s)			
	Grid 3	Grid 2	Grid 1	No Grid
3	3.31	3.33	3.41	3.38
2	2.29	2.27	2.28	2.26
1	1.03	1.10	1.12	1.07

Table 4.1: Actual inlet velocity, U_0 at the reference point(x_0, y_0).

4.1.2. Turbulent Intensity

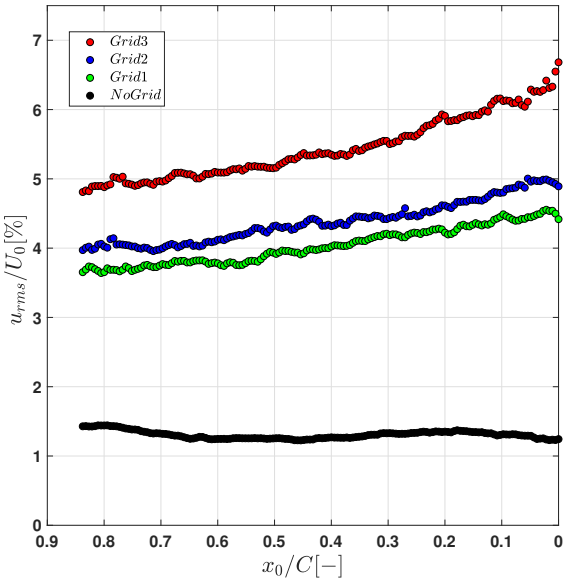

(a) U_{0set} = 3 m/s.

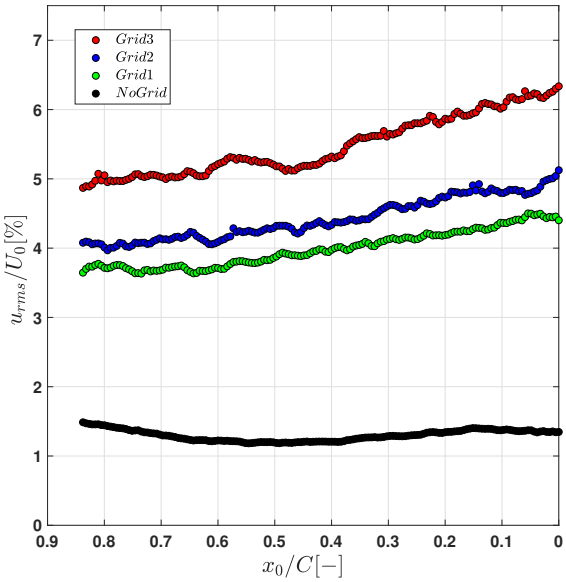

(b) U_{0set} = 2 m/s.

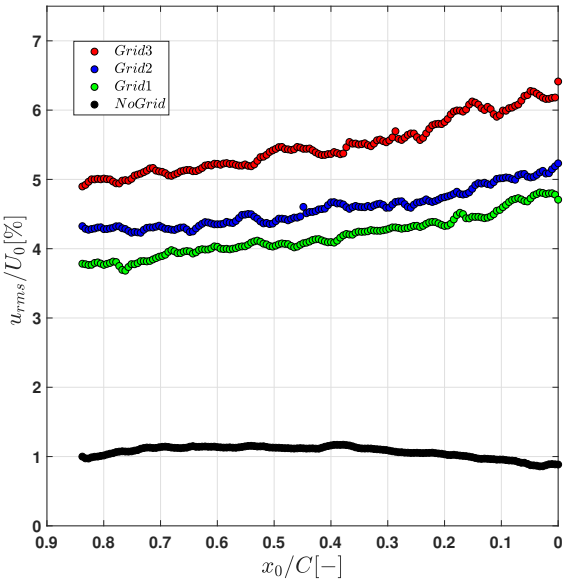

(c) U_{0set} = 1 m/s.

Figure 4.1: Decay of turbulent intensity from reference point (x_0/C), along the downstream distance,x. Figures (a)-(c) show the results for the three different set inlet velocity (U_{0set}) viz: 1 m/s, 2 m/s and 3 m/s respectively. Flow direction is from right to left.

Turbulent intensity (T.I.), defined by

$$T.I. = \frac{u_{rms}}{U_0} \tag{4.1}$$

is used as a parameter to quantify the relative turbulence level downstream of the grid, where u_{rms} is the root-mean-square of the fluctuations in stream-wise velocity component (u'). Decay of turbulent intensity of each grid from the reference point (x_0, y_0) along the downstream distance is shown in figure 4.1a-4.1c. The values of u_{rms} (in m/s) along with the turbulent intensity (T.I.) (in %) at the reference point are given in table 4.2.

Figures 4.1a-4.1c show that the turbulent intensity of NoGrid case is below 1.5%. This is an indication of very low turbulence levels in the mean flow. The long-wave oscillation in the turbulent intensity of NoGrid cases seen in the plots is associated to fluctuations in the bulk velocity. This observation in u_{rms} can also be seen in the contour plot of auto-correlation (ρ_{11}) for NoGrid case shown in figure 4.4d.

Keeping in mind that the porosity, β of all the grids are maintained constant at value of 0.56, a comparison can be made on turbulent intenstity generated by each grid. Grid3 with largest mesh width (M = 32 mm) prodcues the highest turbulent intensity of 6.66 % and Grid1 with smallest mesh width (M = 20 mm) produces lowest turbulent intensity of 4.39 % among the three grids. Study by [26] mentions turbulent intensity of maximum of 10% (at downstream position x/M=10, where x/M=0 refers to location of grid itself) is typically feasible with use of passive grids. This cannot be verified at location x/M = 10 in the current study although emperical relation for decay in turbulent intensity exists (refer equation 2.14). A straight-forward estimation at a desired downstream location is not advisable as the decay exponent and coefficient are highly dependent on initial conditions specifically mesh width (M) and grid porosity (β) [25]. For a simple cross-verification on the order of magnitude of turbulent intensities in present study, literature on grid turbulence was consulted where observations from hot-wire and PIV measurements of [23] and [16] respectively cite turbulence levels of 5.4% and 10.9% at x/M= 20 and x/M= 5 respectively. Inferences from datas of near grid region (x/M<10) turbulent intensity must be done with care as near grid region is highly turbulent and anisotropic from wake of the rods.

Laws & Livesey [26] provides a relation for decay of turbulent intensity along downstream distance X as

$$\frac{U_0^2}{\overline{u'^2}} = b\frac{X - X_0}{M * K} \tag{4.2}$$

where K is a measure of grid solidity (= 1-β) and X_0 is the virtual origin from the grid. Although it is not to be used for exact calculations, above equation says that at constant value of K, turbulent intensity increases with increase in mesh width, M which is observed in the current study (refer table 4.2). It can be seen from table 4.2 that the absolute values of u_{rms} increases with increase in mean inlet velocity (U_0) but the relative percentage (T.I.) stays fairly constanst.

U_{0set} [m/s]	Grid #							
	Grid 3		Grid 2		Grid 1		No Grid	
	T.I. [%]	u_{rms} [m/s]	T.I. [%]	u_{rms} [m/s]	T.I. [%]	u_{rms} [m/s]	T.I. [%]	u_{rms} [m/s]
3	6.66	0.22	4.90	0.16	4.39	0.15	1.2	0.03
2	6.33	0.13	5.12	0.11	4.40	0.10	1.3	0.02
1	6.48	0.06	5.22	0.05	4.70	0.05	0.8	0.008

Table 4.2: Calculated values of u_{rms} and $T.I.$ at the reference point(x_0, y_0).

4.1.3. Integral Length Scales

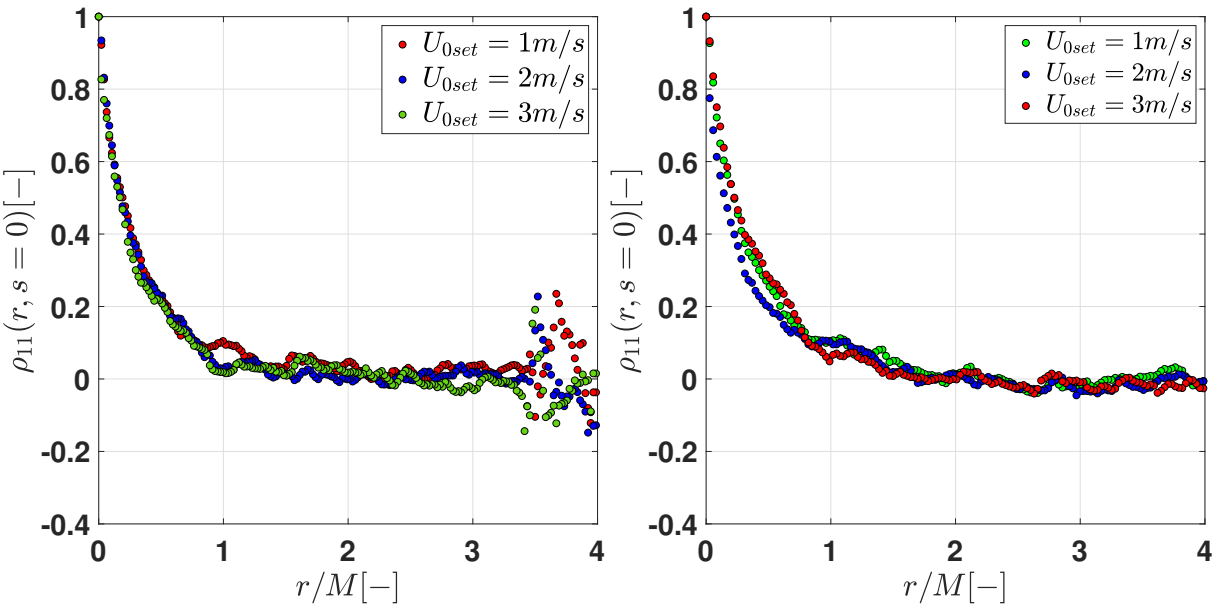

(a) Grid3.

(b) Grid2 .

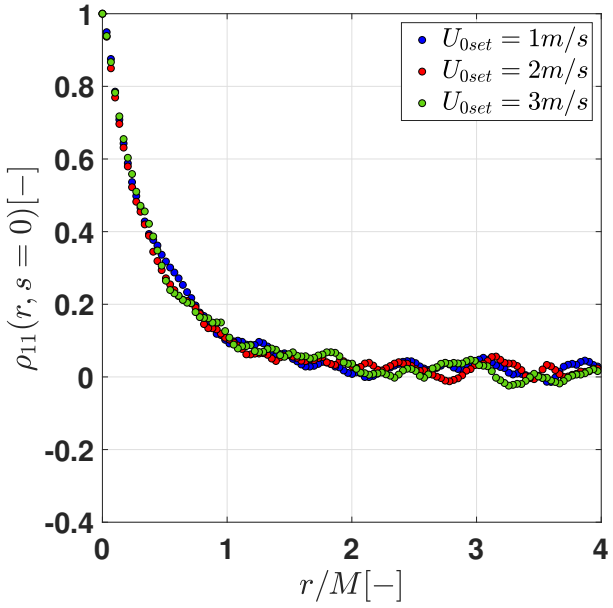

(c) Grid1 .

Figure 4.2: Auto correlation coefficient, $\rho_{11}(r, s = 0)$, computed at the reference point (x_0, y_0). (a)-(c) show the results of Grid3, Grid2, Grid1 cases respectively.

The integral length scale (Λ) in a turbulent flow is a statistical quantity that is calculated using auto-correlation coefficient. This length scale characterizes the range of energy containing eddies in the turbulent flow. For homogeneous, isotropic turbulent flow the 2D

auto-correlation function with x_0, y_0 as reference point is given by

$$\rho_{ij}(r,s) = \frac{R_{ij}(r,s)}{\overline{u_i'(x_0,y_0)^2}} = \frac{\overline{u_i'(x_0,y_0)\,u_j'(x_0+r,y_0+s)}}{\overline{u_i'(x_0,y_0)^2}} \tag{4.3}$$

where r and s represent the physical distance between the 2 points in space at x_0, y_0 and $x_0 + r, y_0 + s$ in x and y direction respectively. When $i = j = 1$ and $s = 0$, R_{11} represents the longitudinal correlation between the stream-wise velocity fluctuations (u') at two locations x_0 and $x_0 + r$. R_{11} when normalised by the variance gives the 1D longitudinal auto-correlation function, $\rho_{11}(r, s = 0)$.

Figures 4.2a-4.2c show the logitudinal auto-correlation coefficient computed at the reference point (x_0, y_0) for each grid. The auto-correlation value has maximum of 1 at the reference point, where $r = 0$, and decreases while moving farther away from it. The sudden fluctuation in $\rho_{11}(r, s = 0)$ for the case of Grid3 (figure 4.2a) is because spurious vectors, which arise due to reflections from laser sheet hitting the hydrofoil, were being considered in computing the auto-correlation coefficient at that location (as $3.7M \approx 12$ cm for M = 32 mm, which is also the distance between the reference point (x_0, y_0) and tip of hydrofoil). The calculation of integral length scale is carried out in manner such that these spurious data are avoided.

The longitudinal integral length scale, Λ_{11} is given by

$$\Lambda_{11} = \int_0^\infty \rho_{11}(r, s = 0)\,dr \tag{4.4}$$

It is to be noted that in equation 4.4, the auto-correlation co-efficient is integrated until infinity. This is not the case in practical situations and in current analysis. In a finite domain, the auto-correlation co-efficient is integrated until the point of first zero-crossing of $\rho_{11}(r, s = 0)$ [28]. The integral length scales computed in such a manner, at the reference point (x_0, y_0), is given in table 4.3

Set inlet velocity,U_{0set} [m/s]	Integral length scale, Λ_{11} [mm]		
	Grid3	Grid2	Grid1
3	11.30	8.84	9.27
2	9.93	7.91	8.90
1	9.70	8.85	9.10

Table 4.3: Integral length scales (Λ_{11}) of each grid computed at reference point(x_0, y_0).

At the first glance the values of integral length scale (Λ_{11}), which scales with mesh width (M) of the grid, seem to be: $\Lambda_{11Grid1} > \Lambda_{11Grid2}$ although $M_{Grid2} > M_{Grid1}$. This is because the considered reference point is at a different scaled downstream position, x/M, for each grid as mesh width, M is different in each grid. The above mentioned values of Λ_{11} of Grid1 is at $x/M = 17$ while for Grid2 is at $x/M = 13$ and Grid3 is at $x/M = 11$ where x/M=0 refers to the position of the grid itself. The downstream development of integral length scales in grid generated turbulence can be understood from generic relation ([23]) given by

$$\frac{\Lambda}{M} = A\Big(\frac{X - X_0}{M}\Big)^m \tag{4.5}$$

where X_0 is the virtual origin of the grid, X is the downstream location from the grid and M is the mesh width of the grid. The coefficient A and exponent m are grid and initial condition dependent parameters.

Generally, the integral length scales in the flow eventually equals mesh width at around from 40 mesh widths or greater[23]. In the current study, the reference point (x_0, y_0) lies close to 17 mesh widths, even for smallest grid (Grid1). This is also the reason why the observed values of integral length scales does not exactly match with the dimension of the mesh width of the grids.

Contours of the 2D auto-correlation coefficient ($\rho_{11}(r,s)$) is one of the ways to visualize the extent of correlation of the turbulent fluctuations. Sample contour plots of auto-correlation (ρ_{11}) of the 3 grids and the no grid condition is shown in figures 4.4a-4.4d. The distinct peak seen in the figures 4.4a - 4.4c for each of the grid case indicates the location of reference point. The correlation value decreases further away from the reference point in either direction. This suggests the existence of a finite correlation distance between the fluctuations of the velocity.

A measure of anisotropy at a point in measurement region can be obtained by calculating the ratio v_{rms}/u_{rms} where v_{rms} is the root-mean-square of fluctuations of the v component of the velocity. The ratio when equal to 1 refers to an isotropic condition and when below 1 suggests fluctuations are more dominant in stream-wise direction. The calculated values of the measure of anisotropy for the current study is shown in table 4.4. The values of v_{rms}/u_{rms} suggest the nearly isotropic nature of the flow downstream of the grids. Figures 4.3a-4.3c shows the evolution of measure of anisotropy along the downstream direction from the reference point (x_0, y_0).

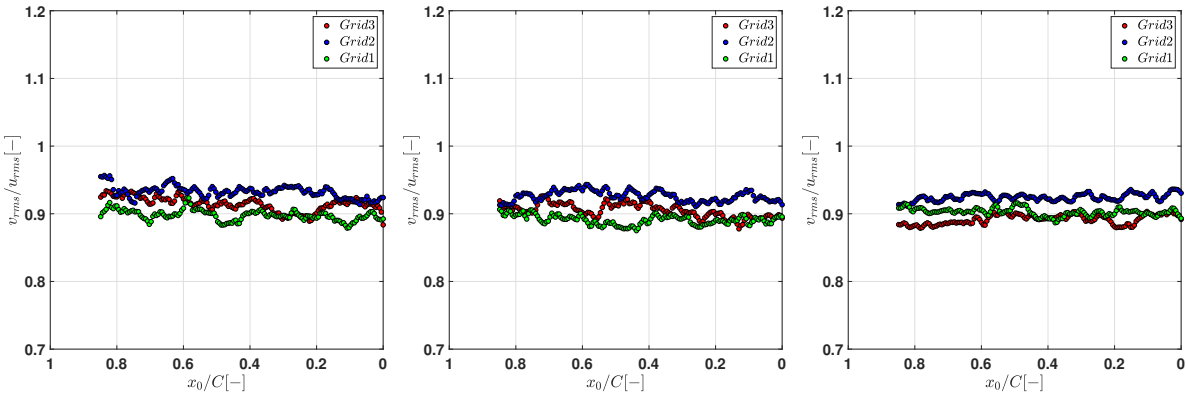

(a) U_{0set} = 3 m/s. **(b)** U_{0set} = 2 m/s . **(c)** U_{0set} = 1 m/s .

Figure 4.3: Evolution of measure of anisotropy, v_{rms}/u_{rms} along the downstream distance, x for each grid computed from the reference point(x_0, y_0). (a)-(c) show results for the set velocity (U_{0set}) at 3 m/s, 2m/s and 1 m/s respectively. Flow direction is from right to left.

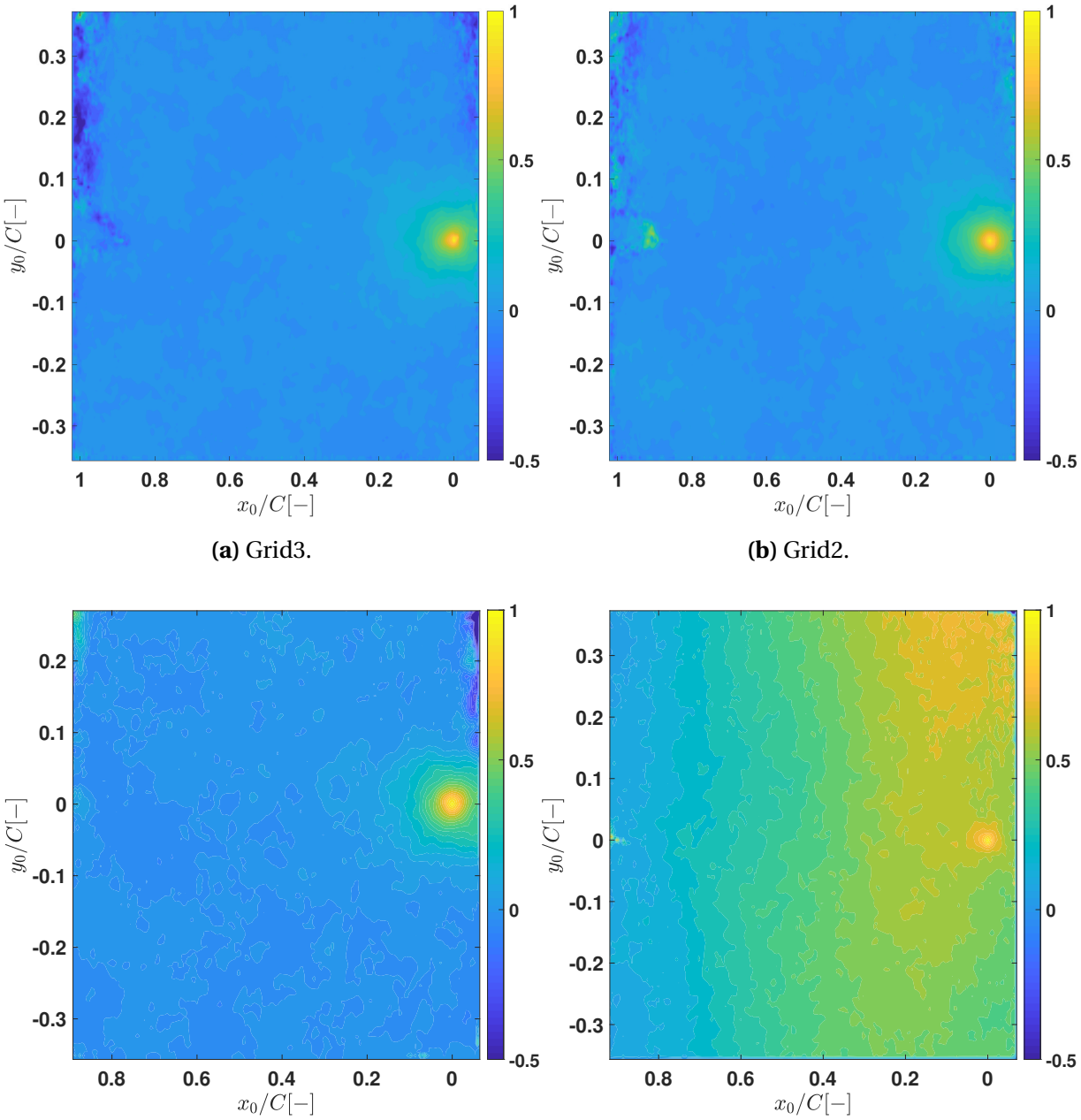

(a) Grid3.

(b) Grid2.

(c) Grid1.

(d) NoGrid.

Figure 4.4: Contour of 2D auto-correlation, $\rho_{11}(r,s)$, computed at reference point(x_0, y_0) for the three grids and no grid conditions. U_{0set} = 3 m/s for all cases. (a)-(d) show results for test cases Grid3, Grid2, Grid1, NoGrid respectively.Flow direction is from right to left.

U_{0set} (m/s)	v_{rms}/u_{rms}		
	Grid3	Grid2	Grid1
3	0.883	0.923	0.892
2	0.893	0.917	0.895
1	0.891	0.930	0.893

Table 4.4: Calculated values of v_{rms}/u_{rms} for each of the grid at reference point (x_0, y_0).

4.2. Vortex Characteristics

In this section, the results of stereo-PIV measurements are presented in two parts.

- Firstly, the effect of upstream turbulence on peak tangential velocity of the tip-vortex is depicted using average tangential velocity ($\overline{v}$ along z at $y = y_{ref} = 0$ and $\overline{w}$ along y at $z = z_{ref} = 0$) profiles. The effect of turbulence on axial velocity ($\overline{u}$ along z at $y = y_{ref} = 0$) is also presented (for a quick and simple visualization refer figure 3.14a and 3.14b).
- Secondly, the effects of the upstream turbulent intensity on vortex centre wandering is shown using probability density function of the difference in tip-vortex's instantaneous and mean centre location.

An estimate of uncertainty in the avaerage velocity components was carried out to the know the quality of the data from experiments. Uncertainty contributions from random erros were estimated for the normalized velocities ($\overline{u}/U_0, \overline{v}/U_0, \overline{w}/U_0$) and shown on each profile with help of errorbars. The procedure employed in calculating the uncertainty from random errors is mentioned below.

- Uncertainty in U_0 was first estimated from the planar PIV measurements. At 95% confidence level, uncertainty δ_{U_0} was calculated using $\delta_{U_0} = 2\,\sigma_{U_0}/\sqrt{N_s}$, where N_s is the number of samples considered for estimating the mean and standard deviation of U_0.
- Similarly, using stereo-PIV measurements, at 95% confidence level unceratinity in the mean of u, v and w were estimated as $\delta_{\overline{u}} = 2\sigma_u/\sqrt{N_s}$, where $N_s = 2000$.
- Also, uncertainty in the root-mean-square of u, v and w were estimated using the relation $\delta_{u_{rms}} = 2\sigma_u/\sqrt{2(N_s - 1)}$.
- Finally, uncertainty in $\overline{u}/U_0$ is estimated as,

$$\frac{\delta_{\overline{u}/U_0}}{\overline{u}/U_0} = \sqrt{\left(\frac{\partial(\overline{u}/U_0)}{\partial\overline{u}} * \delta_{\overline{u}}\right)^2 + \left(\frac{\partial(\overline{u}/U_0)}{\partial U_0} * \delta_{U_0}\right)^2}$$

- Using the same procedures, relative uncertainty was estimated for $\overline{v}/U_0$ and $\overline{w}/U_0$
- The maximum relative uncertainty were found to be around 0.01% in the normalized tangential velocites and 0.5% in the normalized axial velocity.

4.2.1. Average velocity profiles of the tip-vortex

The average velocity profiles of the vortex in the downstream location x/C=0.5 are shown in the following order of test cases: U_{0set} at 3 m/s, 2 m/s and 1 m/s.

The average tangential and axial velocity profiles for the case U_{0set} = 3m/s is shown in figures 4.5a-4.5c followed by a list of inferences.

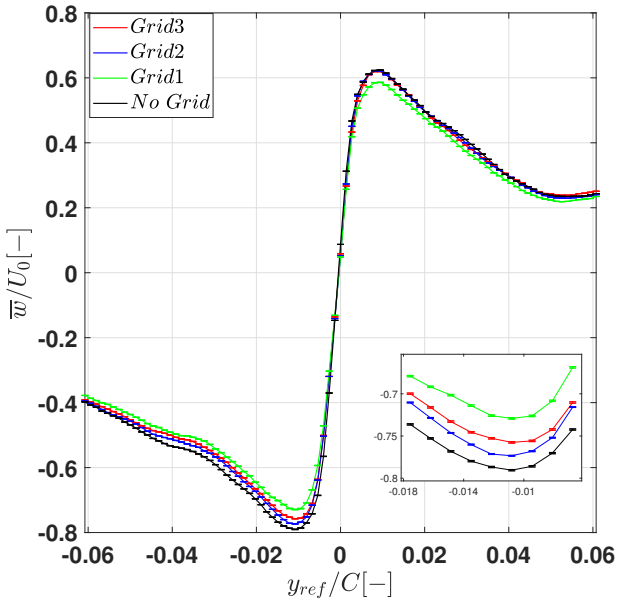

(a) $\overline{w}/U_0$ along y. Inset shows $\overline{w}/U_0$ for $-0.018 < y_{ref}/C < -0.006$.

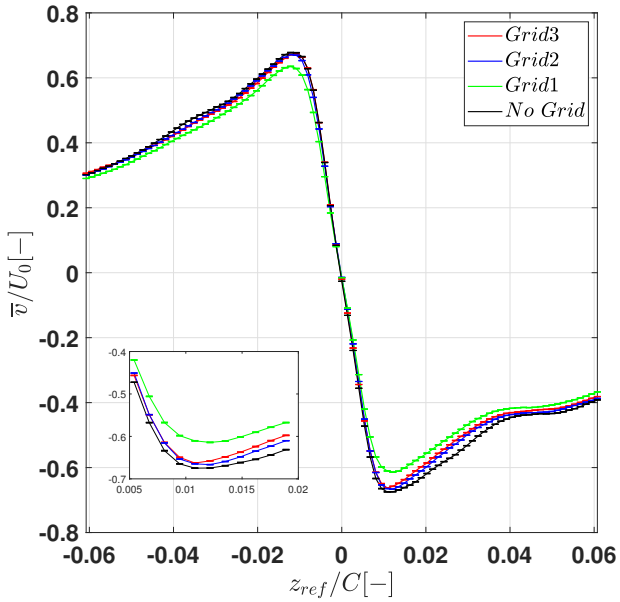

(b) $\overline{v}/U_0$ along z. Inset shows $\overline{v}/U_0$ for $0.005 < z_{ref}/C < 0.02$.

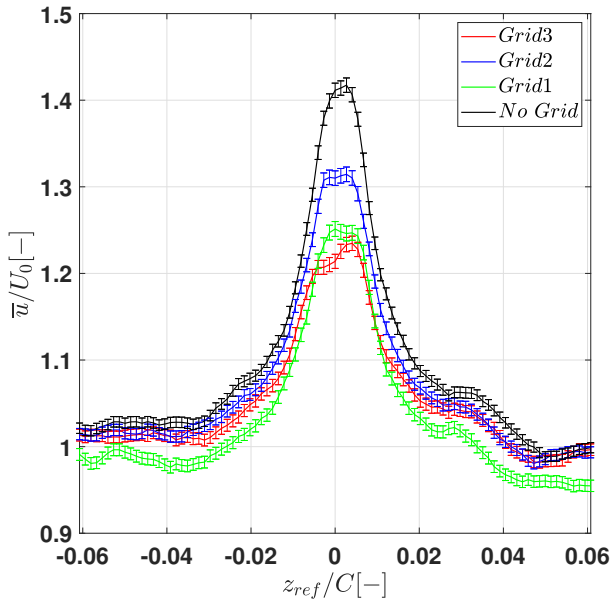

(c) $\overline{u}/U_0$ along z.

Figure 4.5: Average tangential (a and b) and axial (c) velocity profiles of the tip-vortex. Test case:U_{0set} = 3m/s, downstream location: $x/C = 0.5$.

- Reduction of the average peak tangential velocity ($\overline{w}, \overline{v}$) in the grid cases (Grid3, Grid2, Grid1) compared to the No Grid case is not straightforwardly visible. In the current study, a trace of reduction in the peak tangential velocity with increase in turbulent

intensity is observed (refer inset of figures 4.5a and 4.5b for magnitude and trend). A fair comparison of the magnitude of reduction from current results, at downstream location $x/C = 0.5$, with the literature is not completely possible as most of the vortex-turbulence interaction studies were conducted at least a chord length downstream from the tip of the hydrofoil or airfoil. That said, the same trend seen in literature ([9],[18],[14]) where higher reduction in peak tangential velocity is observed for larger incoming turbulent intensity is preserved in the current study except for Grid1. Ideally, it is anticipated that profile of Grid1 to fall between No Grid and Grid2 case as $T.I._{Grid3} > T.I._{Grid2}, T.I._{Grid1} > T.I._{nogrid}$

- Average tangential velocity profiles show that the vortex in not exactly axi-symmetric at this downstream location of $x/C = 0.5$. Clear disctinction can be made on comparing the shape of the velocity profile on either side of the abscissa. In figure 4.5b where the region $0.02 < z_{ref}/C < 0.06$ represents the outboard side of the hydrofoil, the signature of roll-up is seen as an intermittent nearly flat line on the tangential velocity profile at $z_{ref}/C = 0.04$. This location coincides with the location of the spiral in roll-up phase (refer figure 4.6). The location of the spiral as can be seen, is at $z_{ref}/C = 0.04$. Such non-symmetrical vortex profiles in the near-field was also observed in the vortex roll-up investigation by Fruman et al.[41]. In their study, it was observed that roll-up effects on the tangential velocity profile lasted until half a chord length downstream from the tip of the hydrofoil.

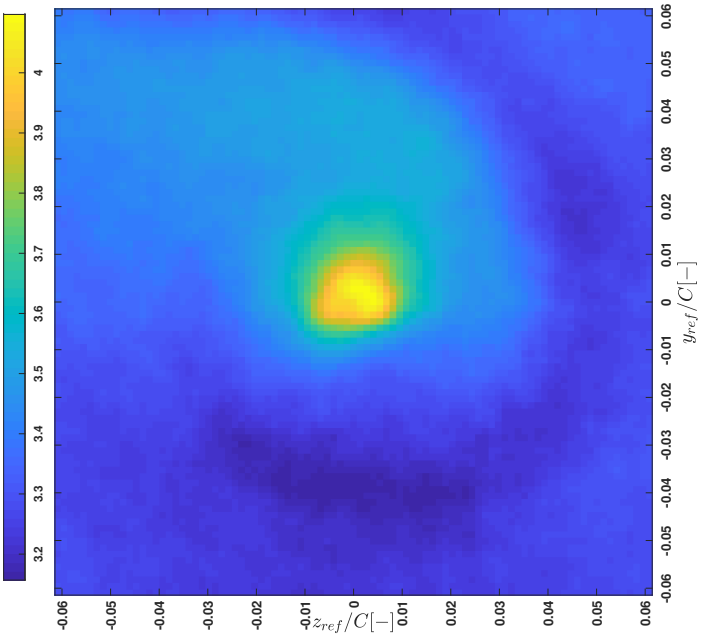

Figure 4.6: Average axial velocity, $\overline{u}$ (in m/s) contour, showing the rollup region in the wake of the hydrofoil. Test case: U_{0set} = 3m/s, downstream location $x/C = 0.5$, Grid3.

- The core of the vortex has a jet-like flow in the axial direction (figure 4.5c). An explanation for the axial acceleration in the core on the basis of inviscid theory is presented

first. Consider a streamline in the core of the vortex that would have orginated from an upstream point where the mean pressure and velocity field is uniform with p_0 and U_0 respectively. At a point in the core of the vortex the Bernoulli fucntion for this streamline can be written as

$$\frac{p_0}{\rho} + \frac{U_0^2}{2} = \frac{p}{\rho} + \frac{{u_x}^2 + {u_\theta}^2 + {u_r}^2}{2} \tag{4.6}$$

where p is the pressure in the core on the corresponding streamline, u_x, u_r and u_θ are axial, radial and tangential component of the velocity vector (in polar coordinate system) respectively. Also, the radial momentum equation in such a flow, after assuming a steady state and axisymmetry of the vortex, can be simplified to

$$\frac{1}{\rho}\frac{\partial p}{\partial r} = \frac{{u_\theta}^2}{r} \tag{4.7}$$

where $u_\theta = \mathcal{K}/r$, $\mathcal{K}$ is the circulation of the vortex.

An expression for the axial velocity in the core can thus be arrived to

$${u_x}^2 = U_0^2 - \frac{\mathcal{K}^2}{r^2} + 2\int_r^\infty \frac{\mathcal{K}^2}{r^3} dr \tag{4.8}$$

$${u_x}^2 = U_0^2 + 4\int_r^\infty \frac{\mathcal{K}^2}{r^3} dr \tag{4.9}$$

The second term in equation 4.9 is always positive inside the core resulting in an axial velocity (u_x) greater than the free-stream velocity. Also, as $r \to 0$,$u_x \to \infty$. The consideration of inviscid theory, where $u_\theta = \mathcal{K}/r$, leads to singularity in tangential and axial velocities as r tends to 0. In real scenarios, the singularity is removed by the action of viscosity by imposing a solid-body like core. For more detailed treatment of axial velocity with inclusion of effects of viscosity, the reader is directed to the work of [40].

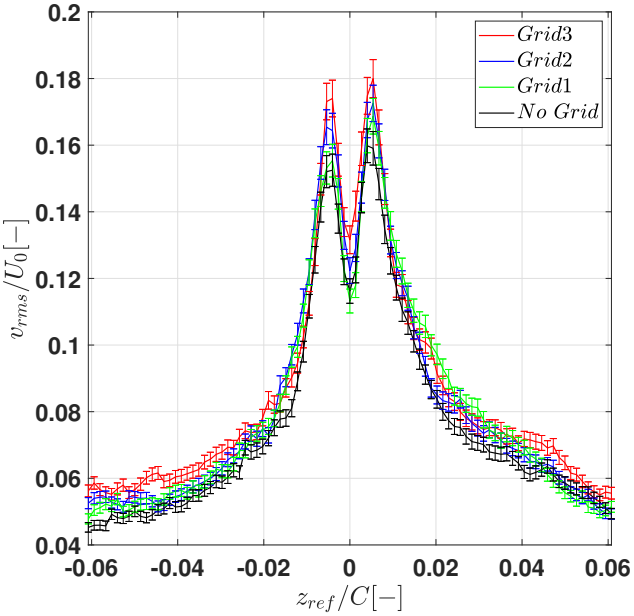

(a) v_{rms}/U_0 along z.

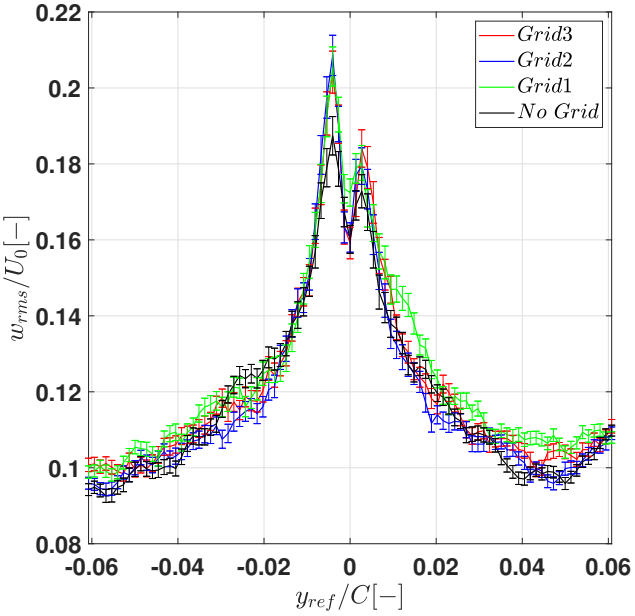

(b) w_{rms}/U_0 along y.

Figure 4.7: Profiles of root-mean-square of the fluctuations of w and v. Test case:U_{0set} = 3m/s, downstream location: $x/C = 0.5$.

- The average axial velocity, at $z_{ref}/C = 0$, reduces from around $1.41U_0$ in No Grid case to $1.31U_0$ in Grid2 case and to $1.22U_0$ in Grid3 case where the inflow turbulent intensity is highest at 6.66%. This shows a significant reduction in the axial momentum of the tip-vortex owing to presence of a turbulent upstream. It can be seen that, axial velocity profile of Grid1 case does not follow a trend as ideally the reduction is anticipated to fall between the No Grid and Grid2 cases. It can also be seen that, further away from the core the axial velocity profiles of all the cases except Grid1 case recovers to free-stream condition ($\overline{u}/U_0 = 1$).

Figures 4.7a and 4.7b shows root-mean-square of fluctuation of v and w component of the velocity. The quantities v_{rms}/U_0 along z and w_{rms}/U_0 along y represent the relative turbulence level along the z and y direction respectively. In the corresponding plots, figure 4.7a and 4.7b, the errorbars of each grid and no grid case overlap with each other. Thus, accurate values cannot be found using these plots. But that said, a qualitative inference can be made by examining the profile. It can be seen that the level of turbulence increases from the axis of the vortex, at $z_{ref}/C = 0$ and $y_{ref}/C = 0$, until it reaches the edge of core of the vortex approximately at $z_{ref}/C = 0.005$ and $y_{ref}/C = -0.004$ for v and w respectively. Moving away from the core of the vortex, the turbulence level reduces significantly and possibly reaches the intensity of free-stream levels. Observations from hot-wire measurements investigating wing tip-vortex under influence of upstream turbulence by Beninati & Marshall [14] shows presence of significant peak in the turbulence levels (v_{rms}^2/U_0^2, w_{rms}^2/U_0^2) in the region just outside of the vortex core. In a phenomenalogical sense, it can be explained that the turbulent intensity peak outside of the core can be due to the fact that the upstream turbulence and turbulence from the wake of hydrofoil may get alinged or wrapped around the primary tip-vortex ([21] [49]) leading to concentrated core of turbulent fluid .

The average tangential and axial velocity profiles of the vortex for U_{0set} = 2m/s is shown in figures 4.8a-4.8c followed by inferences of the results

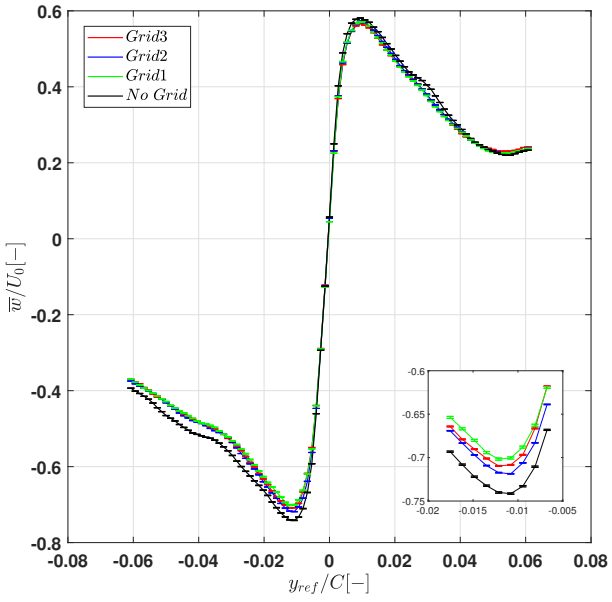

(a) $\overline{w}/U_0$ along y. Inset shows $\overline{w}/U_0$ for $-0.0175 < y_{ref}/C < -0.005$

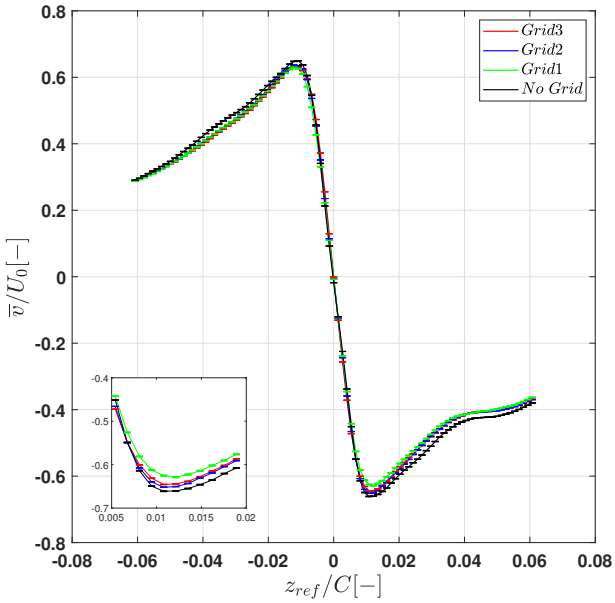

(b) $\overline{v}/U_0$ along z. Inset shows $\overline{v}/U_0$ for $0.005 < z_{ref}/C < 0.02$.

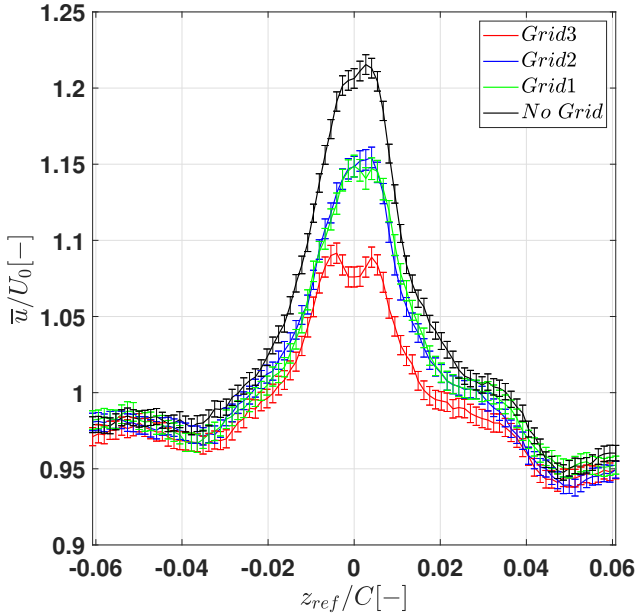

(c) $\overline{u}/U_0$ along z.

Figure 4.8: Average tangential (a and b) and axial (c) velocity profiles.Test case:U_{0set} = 2m/s, downstream location: $x/C = 0.5$.

- The trend observed in the reduction of peak tangential velocity in the case of U_{0set} = 2m/s (refer inset of figures 4.8a and 4.8b) is similar to the one observed in U_{0set} =

3m/s. Reducing the Reynolds number, based on chord length (C), by changing U_{0set} from 3m/s to 2m/s does not seem to have a significant effect on tangential velocity of the vortex. The test cases of Grid1 seems to be an outlier again in this set inlet velocity of 2m/s as profile of Grid1 case must ideally lie between NoGrid and Grid2 case given that $T.I._{Grid3} > T.I._{Grid2}, T.I._{Grid1} > T.I._{nogrid}$.

- Again, the signature of vortex roll-up is seen as intermittent nearly flat line at $y_{ref}/C = -0.04$ and $z_{ref}/C = 0.04$ in the average w and v velocity profiles. Figure 4.9 shows the roll-up phase downstream of the hydrofoil. The location of the spiral matches with the location of flat line in the average tangential velocity profiles, resulting in a non-symmetrical vortex.

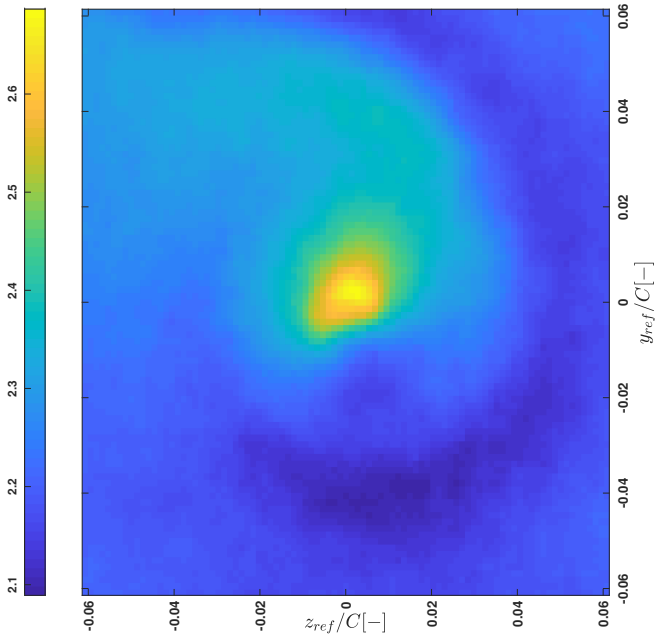

Figure 4.9: Average axial velocity, $\overline{u}$ (in m/s) contour, showing the rollup region in the wake of the hydrofoil. Test case: U_{0set} = 2m/s, downstream location $x/C = 0.5$, Grid2.

- From figure 4.8c, presence of jet like flow in the core of the vortex is also apparent. The mean axis line velocity, at $z_{ref}/C = 0$, is $1.21U_0$ for NoGrid case while $1.15U_0$ for Grid2 and $1.08U_0$ for Grid3 case. The case of Grid1 is almost identical to Grid2 case which is not in accordance with literature as Grid1 case is aniticipated to lie between NoGrid and Grid2 case considering the turbulent intensity produced by the grids.

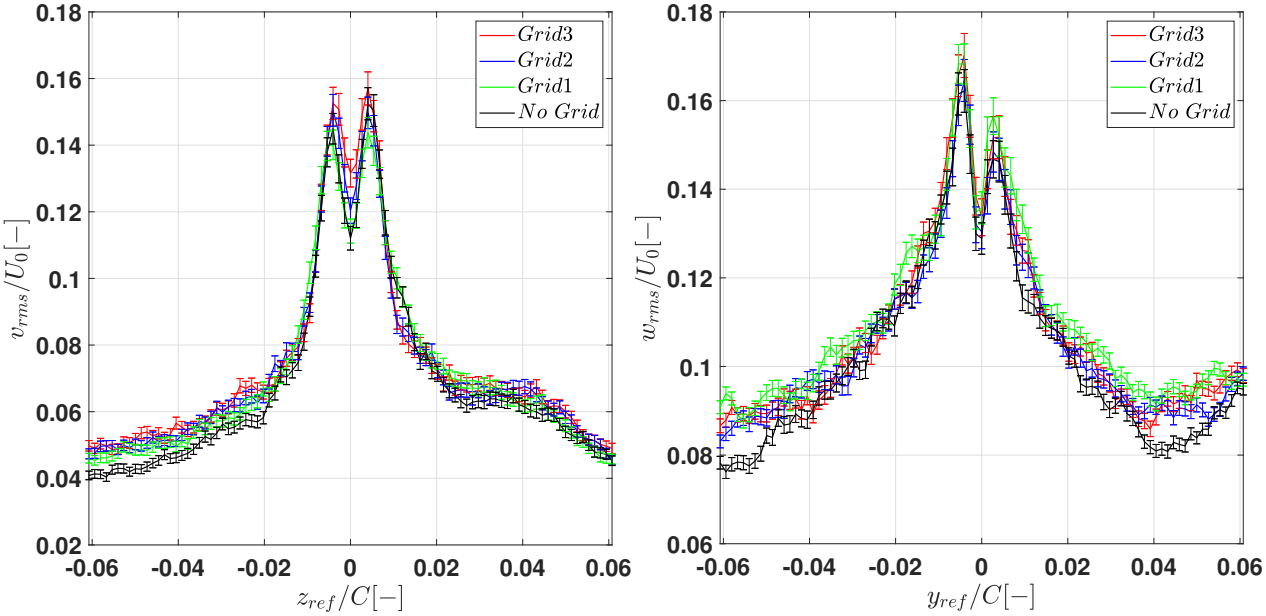

(a) v_{rms}/U_0 along z.

(b) w_{rms}/U_0 along y.

Figure 4.10: Root-mean-square of the fluctuations of v and w. Test case:U_{0set} = 2m/s, downstream location: $x/C = 0.5$.

Figures 4.10a and 4.10b shows root-mean-square of fluctuation of v and w component of the velocity. As mentioned earlier in the case of U_0 = 3m/s, only a qualitative inference can be made from the presented plots owing to the magnitude of uncertainty in the rms values of v and w. As it is seen from the plots, the relative turbulence levels indicated by v_{rms}/U_0 and w_{rms}/U_0 peak at the end of the core region approximately at $z_{ref}/C = 0.006$ and $y_{ref}/C = -0.004$ respectively.

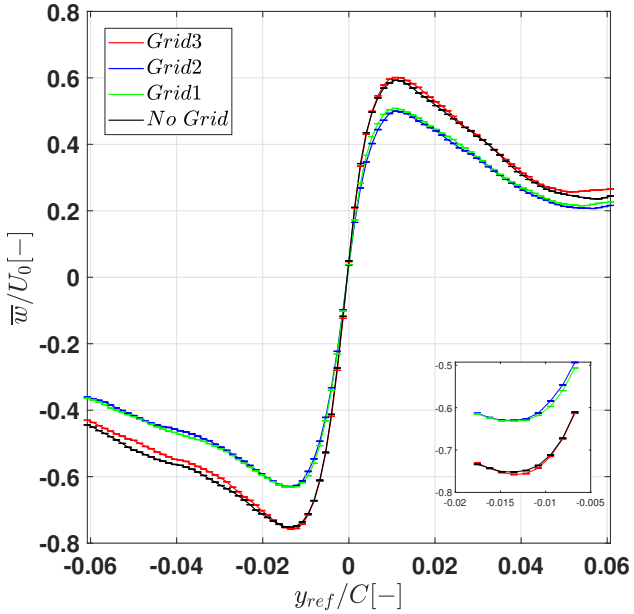

(a) $\overline{w}/U_0$ along y.

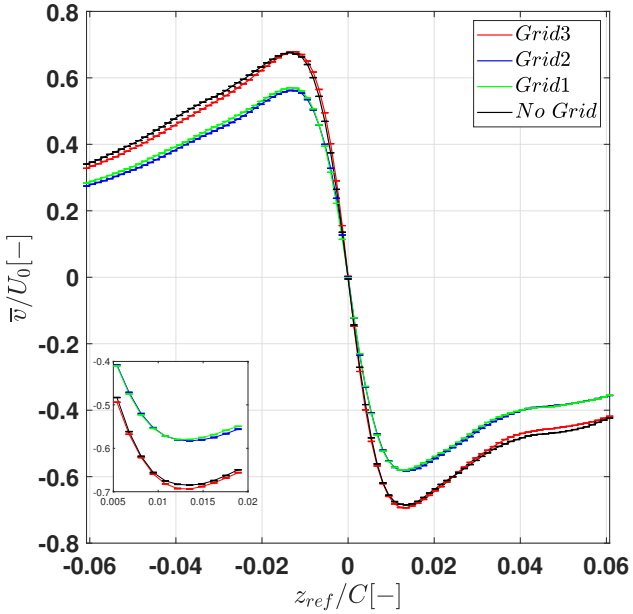

(b) $\overline{v}/U_0$ along z.

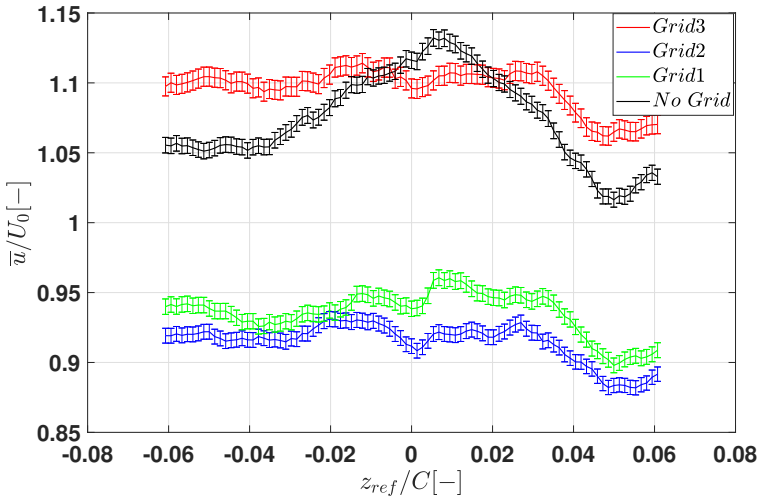

(c) $\overline{u}/U_0$ along z.

Figure 4.11: Average tangential (a and b) and axial (c) velocity profiles.Test case:U_{0set} = 1m/s, downstream location: $x/C = 0.5$.

The average tangential and axial velocity profiles of the vortex at U_{0set}= 1m/s are shown in figures 4.11a-4.11c followed by a list of inferences from the results obtained.

- The reduction in peak tangential velocity seems to be over-estimated in this case. The observed velocity profile maybe due to a measurement artefact where the measured velocity vectors might have taken a biased value leading to distinct separation between each case.

- Although the roll-up is visible (refer figures 4.12a -4.12d), presence of a disticnt core cannot be seen as observed in the previous two cases (refer figures 4.6 and 4.9).

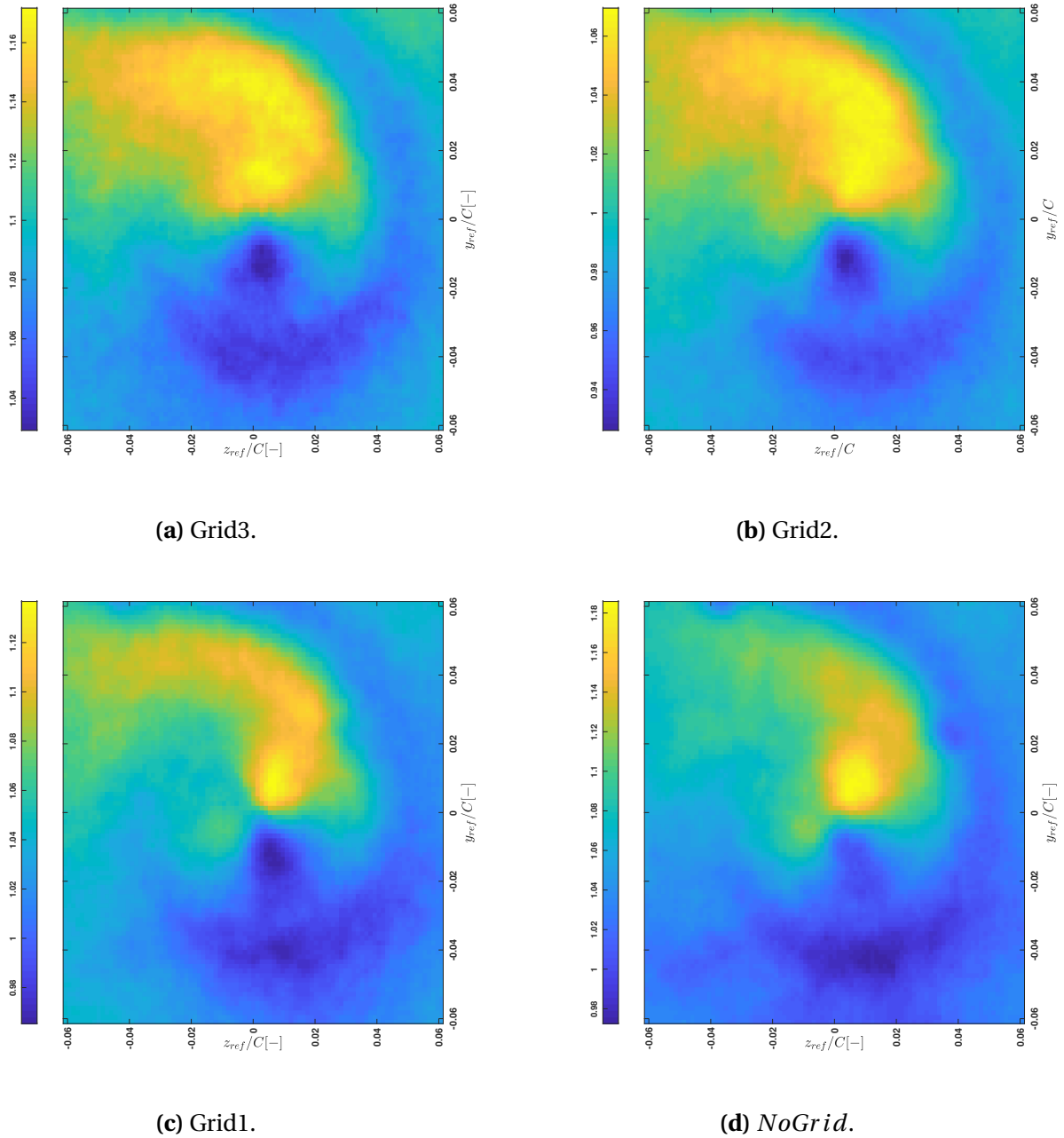

(a) Grid3.

(b) Grid2.

(c) Grid1.

(d) $NoGrid$.

Figure 4.12: Average axial velocity, $\overline{u}$ (in m/s) contour, showing the rollup region in the wake of the hydrofoil. Test case: U_{0set} = 1m/s, downstream location x/C = 0.5. (a)-(d) show the results of each grid and the no gird case.

Figures 4.13b and 4.13a show the profiles of root-mean-square of the fluctuations in v and w component of the velocity. The measurement artefact as mentioned in inferences along with uncertainty does not allow to make inferences on the observed profiles in the plots with confidence. No further physics based inferences are made on the datasets at U_{0set} = 1m/s.

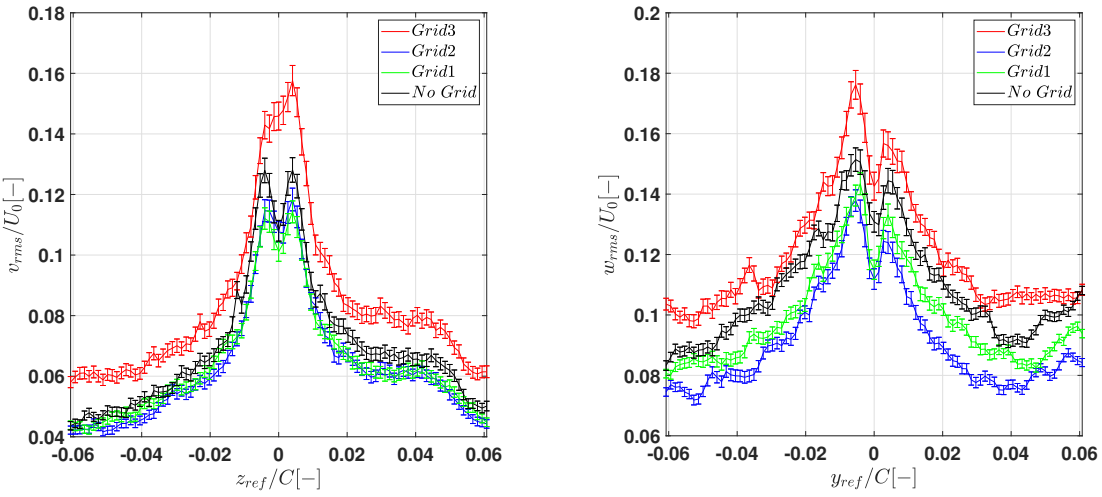

(a) v_{rms}/U_0 along z. **(b)** w_{rms}/U_0 along y.

Figure 4.13: Root-mean-square of the fluctuations of v and w component of velocity. U_{0set} = 1m/s. Downstream location: $x/C = 0.5$.

4.2.2. Vortex characteritics at second downstream position, x/C=1.3

Average tangential velocity profiles of the tip-vortex at the downstream location $x/C = 1.3$ are shown in figures 4.14a and 4.14b followed by few important observations.

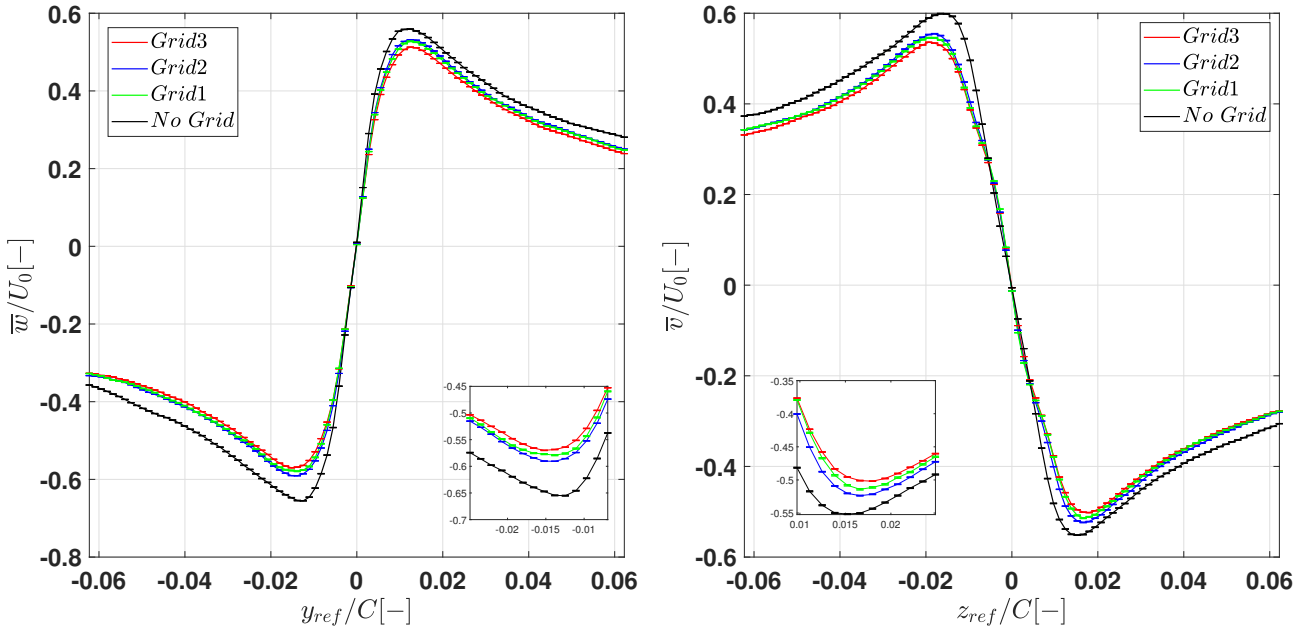

(a) $\overline{w}/U_0$ along y. Inset shows $\overline{w}/U_0$ for -0.025 < y_{ref}/C < -0.0075.

(b) $\overline{v}/U_0$ along z. Inset shows $\overline{v}/U_0$ for 0.01 < z_{ref}/C < 0.025.

Figure 4.14: Average tangential velocity profiles. Test case:U_{0set} = 2m/s, downstream location: $x/C = 1.3$.

- Signature of roll-up on the velocity profiles as observed at $x/C = 0.5$ is not seen here leading to nearly axisymmetric profile of the vortex.
- The reduction in the peak tangential velocities are more prominently seen compared to the test cases at $x/C = 0.5$. More importantly, the radial location of the peak (refer inset in figures 4.14a and 4.14b) in each of the grid case and no grid case is clealy distinguishable and does not occur at same radial position (refer table 4.5). The peak velocity in Grid3 case occurs further away from the vortex centre compared to NoGrid case (refer 4.15). This is indicative of tangential velocity decay being enhanced by the upstream turbulence. But, such clear separation was not observed in the tangential velocity profiles at the location $x/C = 0.5$.

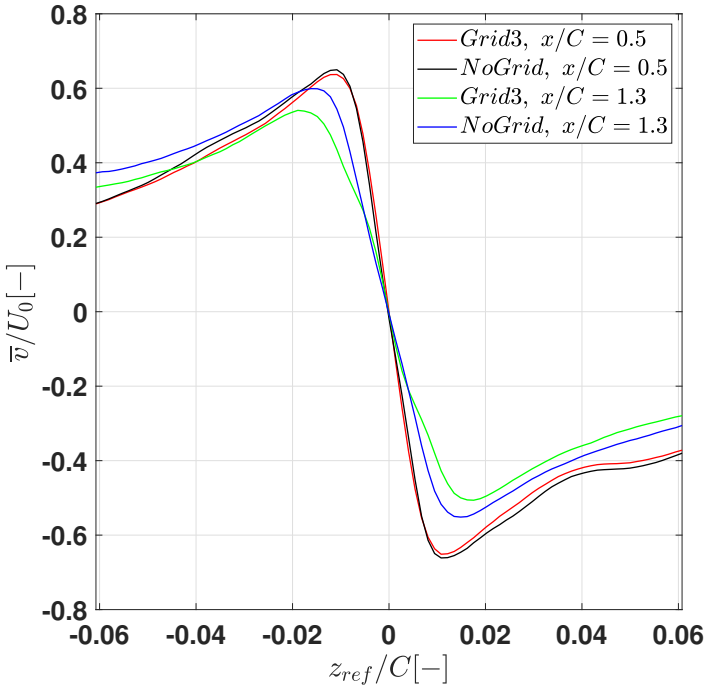

Figure 4.15: Comparison of tangential velocity profile ($\overline{v}/U_0$) of the vortex at $x/C = 0.5$ and $x/C = 1.3$.

- Holzapfel et al. [21] explains possible mechanism happening in the hindsight that leads to vortex decay enhancement by upstream turbulence. The incoherent vortices in the upstream turbulence are sucked and coiled around the tip-vortex forming secondary vortical structures. These azimuthally aligned secondary vortices are intensified by the tip-vortex due to stretching thereby transferring energy to the secondary vortices. The intensified secondary vortices farther downstream lead to decay and deformation of the tip-vortex. Also, Ghimire & Bailey [43] showed existence of intermittent rapid reduction in circulation of a tip-vortex with turbulent upstream. They also show the presence of vortex stripping process, where the core fluid being ejected out by the azimuthally aligned coherent vortex structures at downstream location x/C =6.5 to 8. The reader is directed to Appendix A where supportive information is provided on the signatures of these structures observed in this thesis.

- A comparitive summary of location of the peak in the $\overline{v}/U_0$ profile of two downstream locations when U_{0set} = 2m/s is given in table 4.5. The location of the peak with reference to the vortex centre is identified using z_{ref}/C in $\overline{v}/U_0$ velocity profile. For the case of $x/C = 1.3$, the radial location of the peak moves farther away from the vortex centre with increase in turbulent intensity in contrast to the cases at $x/C = 0.5$.

Downstream location	Radial location of peak tangential velocity (z_{ref}/C)			
	No Grid	Grid3	Grid2	Grid1
$x/C = 0.5$	0.0108	0.0108	0.0108	0.0121
$x/C = 1.3$	0.0152	0.0179	0.0166	0.0166

Table 4.5: Radial location of the peak tangential velocity observed at the two downstream location $x/C = 0.5$ and $x/C = 1.3$. Test case: U_{0set} = 2m/s.

4.2.3. Vortex wandering

The wandering of vortex centre is quantified using probability density function of the difference between instantaneous and mean vortex centre position. The amplitude of the vortex centre wandering about the mean centre position can be understood from the the spread of the PDFs. With increase in upstream turbulent intensity, the amplitude of wandering increases. This is evident from figures 4.16a, 4.17a and 4.18a where a clear trend is observed. The spread of PDF is highest for the case of Grid3 and lowest for NoGrid case. Also, the amplitude does not change significantly with increase in mean inlet velocity. In the current study, a weak Reynolds number (based on chorld length,C) dependence in the amplitude of the wandering is observed. Examining the spread of the PDFs of horizontal and vertical wandering shows that the wandering amplitude is higher in the horizontal direction (along z axis) than in vertical direction (along y axis).

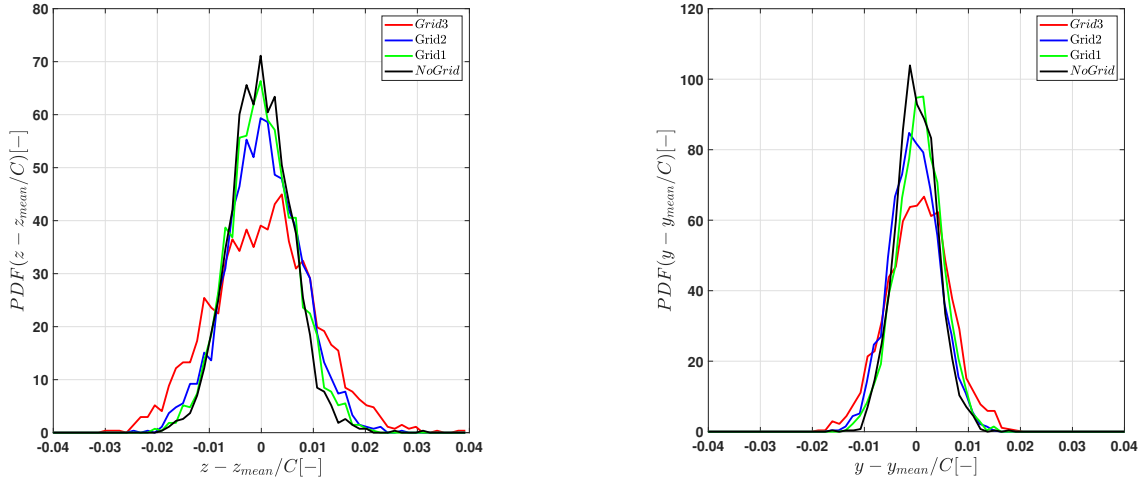

(a) Horizontal wandering.

(b) Vertical wandering.

Figure 4.16: Probability density function of the difference between instantaneous and mean vortex centre position (normalised).(a) shows the PDF of vortex centre wandering along z directon and (b) shows the PDF of vortex centre wandering along y directon. Test case:U_{0set} = 3m/s, downstream location: $x/C = 0.5$.

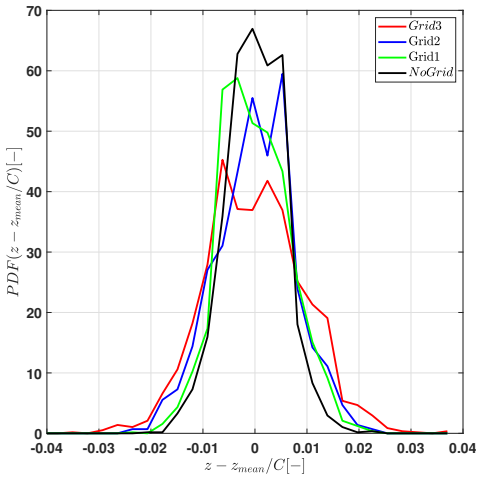

(a) Horizontal wandering.

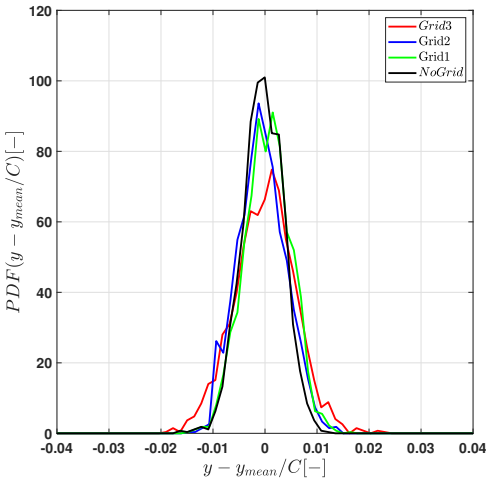

(b) Vertical wandering.

Figure 4.17: Probability density function of the difference between instantaneous and mean vortex centre position (normalised).(a) shows the PDF of vortex centre wandering along z directon and (b) shows the PDF of vortex centre wandering along y direction. Test case:U_{0set} = 2m/s, downstream location: $x/C = 0.5$.

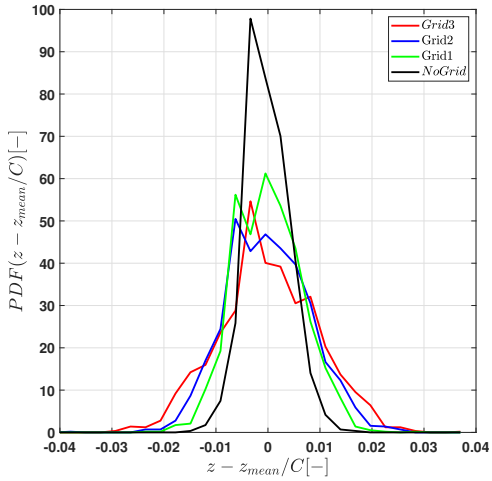

(a) Horizontal wandering.

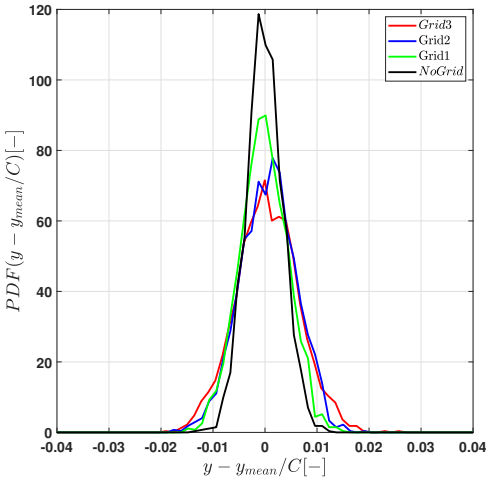

(b) Vertical wandering.

Figure 4.18: Probability density function of the difference between instantaneous and mean vortex centre position (normalised).(a) shows the PDF of vortex centre wandering along z directon and (b) shows the PDF of vortex centre wandering along y directon. Test case:U_{0set} = 1m/s, downstream location: $x/C = 0.5$.

The standard deviation, σ_y and σ_z, of instantaneous vortex centre location is representative of the amplitude of the vortex wandering in y and z direction respectively. Since from the initial observations it is seen that amplitude is higher along z-direction, only the standard deviation σ_z is summarized and further explored. Table 4.6 shows the standard

U_{0set} [m/s]	Measure of amplitude of wandering (σ_z/C)			
	Grid3	Grid2	Grid1	No Grid
3	0.0104	0.0071	0.0064	0.0059
2	0.0094	0.0075	0.0066	0.0055
1	0.0094	0.0078	0.0064	0.0043

Table 4.6: Standard deviation of instantaneous vortex centre positions normalized by chord length, C. Data obtained from measurements at $x/C = 0.5$

deviation of vortex centre location, normalized by chord length C, obtained from the measurements performed at $x/C = 0.5$.

Interestingly, the measure for amplitude of wandering (σ_z/C) for Grid3 is close to the size of the vortex core (refer table 4.5, $x/C = 0.5$) which was also observed in previous studies[44].

5

Conclusions and recommendations

This chapter summarises the investigation carried out in this thesis in section 5.1. The research questions formulated in the beginning of this investigation are answered with supporting statements in section 5.2. Finally, some recommendations for future work is given in section 5.3

5.1. Summary

The effect of the upstream grid generated turbulence on a tip-vortex from a NACA 66_2-415 hydrofoil was studied using stereo-PIV measurement technique. As a pre-requisite, the inflow condition to hydrofoil was characterized using the parameteres turbulent intensity and streamwise integral length scales (Λ_{11}) with help of planar PIV measurements. The response of tip-vortex to three different upstream turbulent intensities was shown through average tangential and axial velocity profiles. This response was compared with a baseline condition where no grid was used. Also, the vortex centre wandering was quantified by computing the probability density function of the difference between instantaneous and mean vortex centre poisition.

5.2. Answering reasearch questions

- *How is the average peak tangential velocity of the tip-vortex altered under turbulent inflow condition compared to a uniform inflow condition ?*

  - The magnitude of the effect of the upstream turbulence on tip-vortex depends on the downstream location of investigation. At a location 0.5 chord length downstream from the tip of the hydrofoil, the strength of the tip-vortex is significantly high compared to the energy in the free-stream turbulence. A significant effect on the magnitude of the peak tangential velocity is not observed. Travelling further downstream, at a distance more than a chord length, a significant reduction in the magnitude of peak tangential velocity with increase upstream turbulent intensity can be observed. A mechanism behind such process is presented in the work of Holazapfel et al. [21]. The incoherent vortical structures in the turbulent free-stream are initially drawn in and wrapped around the tip-vortex to form azimuthally aligned coherent secondary vortices.

Over the downstream distance, the coherence and intensification in these secondary structures is achieved by stretching and tilting of secondary vortices by the strong primary tip-vortex. This consumes the energy of the primary vortex. Consequently, from here, these intensified secondary vortices distort and decay the primary vortex faster.

– The above mentioned mechanism is feasible provided the secondary structures alingn azimuthally around the primary vortex so that they can get stretched and intensified. PIV measurements by Ghimire & Bailey [43] expose the presence coherent secondary structures around the primary tip-vortex. Also, Beninati & Marshall [14] observed the presence of highly turbulent region around the core of the vortex. This can be possible when the free-stream turbulence in some way surrounds the primary tip-vortex. Thus, in the presence of turublent inflow to a hydrofoil, the tip-vortex decay is enhanced by the upstream turbulence resulting in reduction in the magnitude of the peak tangential velocity. Traces of signature of secondary vortical structures observed in this thesis could be seen in figure 2b, Appendix-A.

- *How does the turbulent inflow condition affect the wandering of vortex centre?*

  – The amplitude of vortex centre wandering from its mean position in seen to directly relate with the level of turbulent intensity at the inflow. The spread of the PDFs of the vortex centre wandering proves this statement. This observation was in accordance with previous studies on wandering by [9] , [45] , [44]. Also, the amplitude of wandering was found to be higher in the spanwise direction compared to the lift direction and roughly scaled with the size of the vortex core at highest turbulent intensity (Grid3). PDF of vortex centre wandering in the downstream position x/C = 1.3 could not be thouroughly investigated with limited availability of dataset. Thus no definitive conclusion was made from the available dataset at the location x/C = 1.3. The PDF obtained for the available dataset at x/C = 1.3 is provided in Appendix-A.

5.2.1. Additional conclusion

In the average axial velocity profiles ($\overline{u}/U_0$) presented in section 4.2.1, for the test cases of U_0=3m/s and 2m/s, a significant reduction in axial velocity at the vortex axis ($z_{ref}/C = 0$) was observed for the test cases of Grid3 and Grid2 compared to NoGrid condition. This leads to a significant reduction in local axial acceleration inside the core of the vortex.

5.3. Recommendations for further study

A list of recommendations are mentioned below to carry forward from the learning of the current study.

- In the current experiments, as only mean velocity profiles of tip-vortex was of primary interest, turbulence statistics inside the core could not be measured with high level of accuracy. For extension of investigation on the current topic, it would be

worth while to measure the turbulent stresses inside and around the core which can throw light on the transport of momentum inside the core of the vortex. This can help to have a concrete answer to the decrease in the axial velocity of the tip vortex that was observed when grids were placed upstream of the hydrofoil.

- Secondary vortices, if for sure is, aligned in the azimuthal direction, could not be captured in the current study due to the design of the experimental setup where only inplane values could be measured. A volumetric velocity field measurement around the tip-vortex can give us information on the azimuthal vorticity which can be used to further investigate the presence and the action of secondary vortical structures on the tip-vortex.
- In the current study, the turbulent intensity of the three grids were varied only within few percentages. A wider spectrum of with larger step sizes between each turbulent intensity should be analysed to see a clearer impact of the magnitude of turbulent intensity on the decay of the tip-vortex.

Appendix-A

A.1 Traces of secondary vortical structures

Additional information on the signatures of secondary vortical structures ([21], [49] , [43]) observed in the current thesis is given below. Instantaneous velocity magnitude contours are presented for the case of Grid3 and NoGrid case at the two planes $x/C = 0.5$ and $x/C = 1.3$.

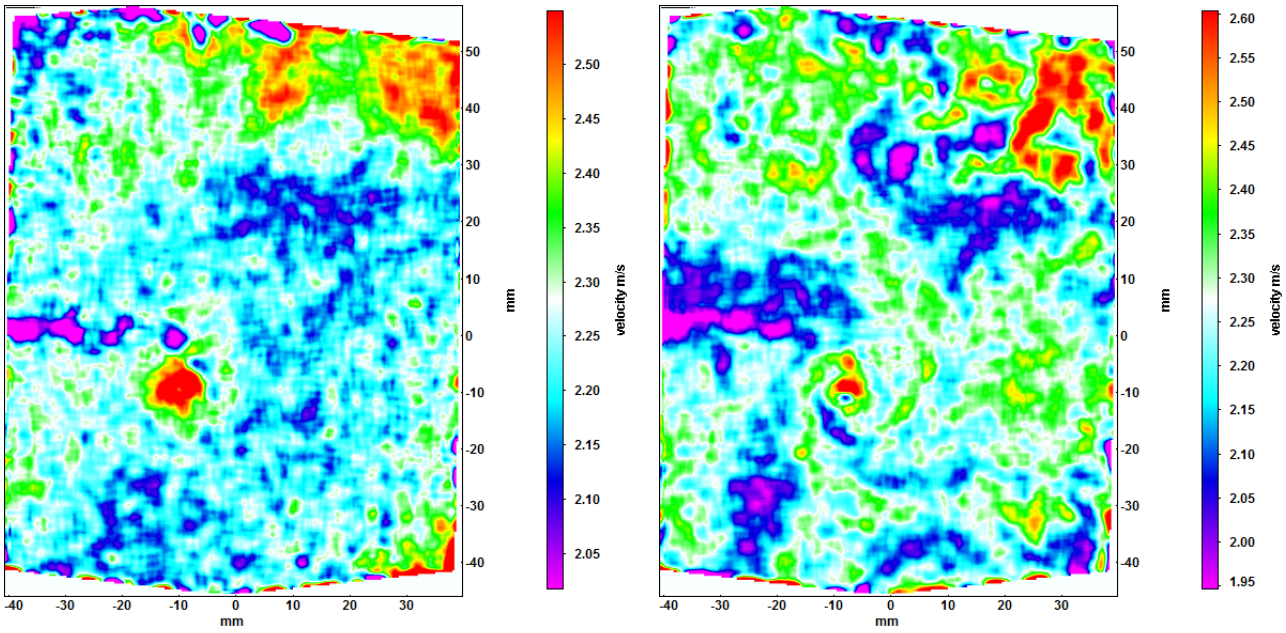

(a) Test case: No Grid.

(b) Test case: Grid3.

Figure 1: Instantaneous velocity magnitude contours of the tip-vortex. U_{0set} = 2m/s. Downstream location: x/C =0.5. Direction of rotation of tip-vortex is in clock-wise direction.

As mentioned by [21],[49], the less coherent upstream vortrical structures are first wrapped around the tip-vortex. These vortical structures, over time, get stretched and tilted thus intensified in vorticity. Travelling further downstream, they drive faster decay of the tip-vortex compared to a condition where there is minimal or not so significant intensity of background turbulence. The secondary structures get more coherent at $x/C = 1.3$ than at $x/C = 0.5$ which can be seen from figures 1b and 2b .

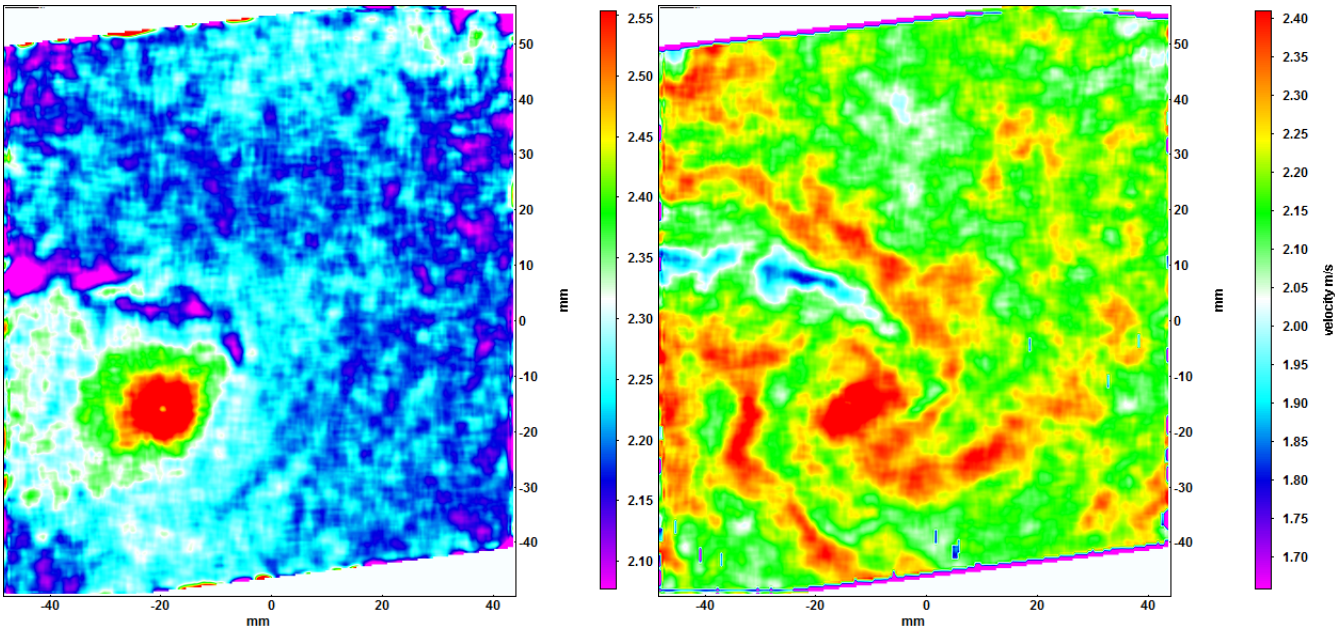

(a) Test case: No Grid.

(b) Test case: Grid3.

Figure 2: Instantaneous velocity magnitude contours of the tip-vortex. U_{0set} = 2m/s. Downstream location: x/C =1.3.Direction of rotation of tip-vortex is in clock-wise direction.

The signature of these vortical structures is not found in the test case of NoGird where the background turbulent intensity is around 1.3% comapared to 6.33% in Grid3 case.

A.2 Vortex wandering at downstream location x/C=1.3

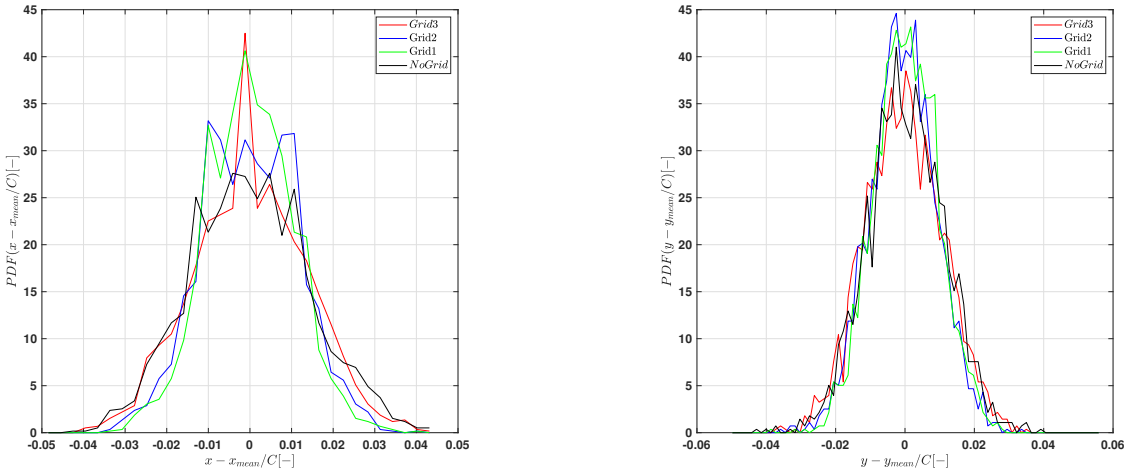

(a) Horizontal wandering.

(b) Vertical wandering.

Figure 3: Probability density function of difference between instantaneous and mean vortex position (normalised).(a) shows the PDF of vortex centre wandering along z directon and (b) shows the PDF of vortex centre wandering along y directon U_{0set} = 2m/s. Downstream location: x/C =1.3

Figure 3a shows the PDF of difference between intantaneous and mean vortex centre position. It can be seen that the width of spread is increased to $z - z_{mean}/C = 0.04$ in this downstream location compared to $z - z_{mean}/C = 0.03$ at $x/C = 0.5$. Previous experimental observations [44] [9] also show that with decay of circulation, the wandering amplitude increases. But, the amplitude conincides or falls close to each other for all grid cases which means no dependency on the turbulent intensity. Intuituvely and also in accordance to literature, this does not match with previous observation. Thus the author does not want to give a conclusive remark on this observation.

Appendix-B

This appendix presents some additional information related to the experimental campaign.

Figure 4 shows the camera arrangement of planar PIV and stereo PIV measurement. Planar and stereo-PIV experiments were done as two different campaigns. Figure shows setup of both only for quick understanding.

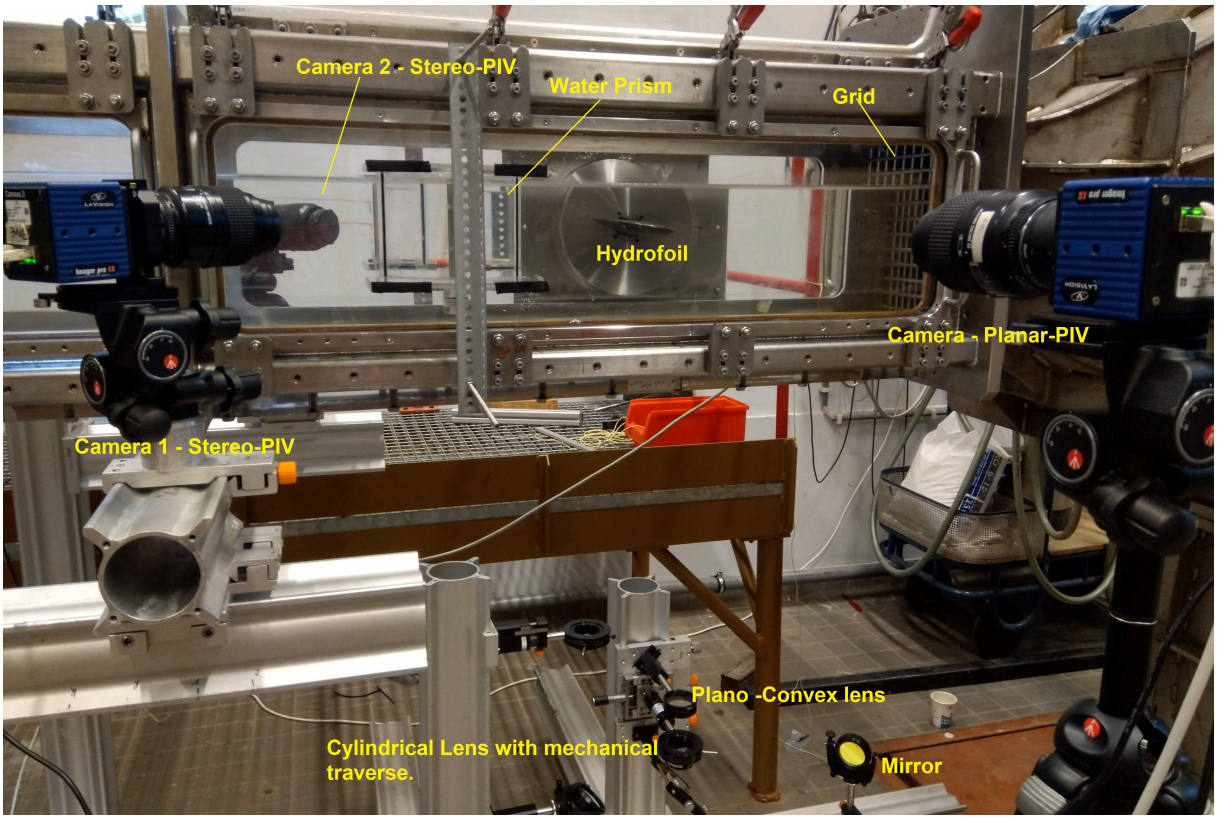

Figure 4: Figure showing the camera arrangement for stereo and planar PIV experiments.

The calibration target (Type-11) from LaVision ©used in the calibration of cameras during planar and stereo PIV experiments is shown in figure 5

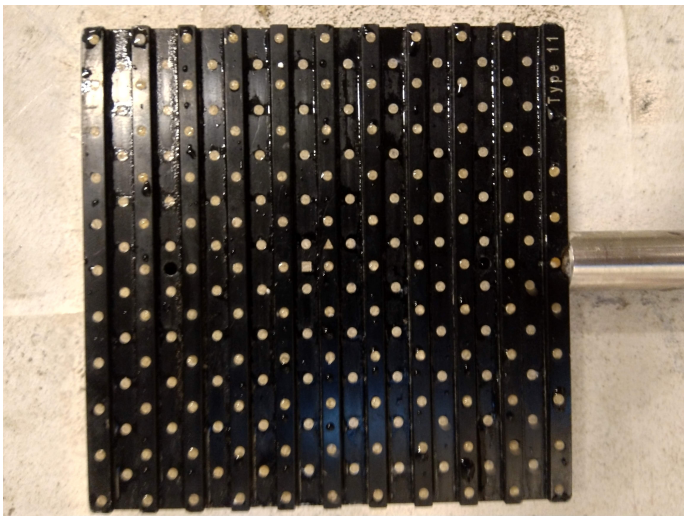

Figure 5: Type-11 target plate used during the PIV experiments for calibration of the cameras.

Figure 6 below shows the calibration curve of the differential pressure sensor that was used to control the cavitation tunnel inlet velocity.

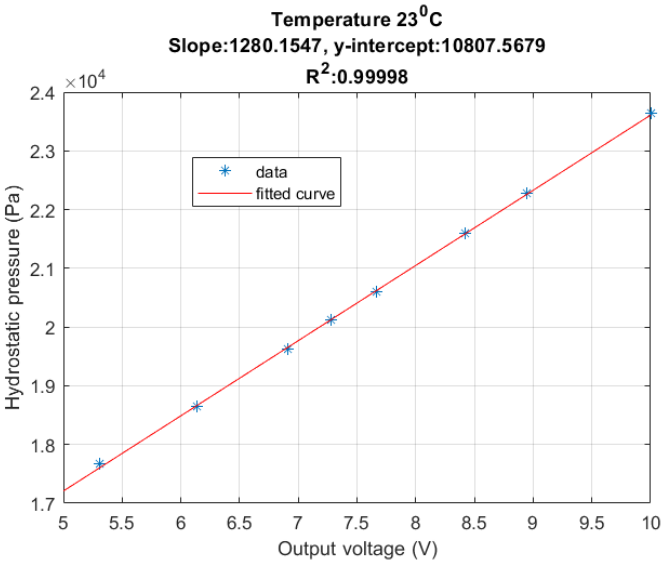

Figure 6: Calibration details of the differential pressure sensor used to control the tunnel free-stream inlet velocity

Figure 7: The differential pressure sensor that was used in the current test setup to control the tunnel free-stream inlet velocity.

Investigation for convergence of statistical quantity (u_{rms}) was carried out to check if the number of image samples taken (2000) are enough for the convergence of statistical quantities. Study carried out using data obtained from planar PIV measurements of Grid3 and Grid2 at 3m/s is show in figures 8a and 8b .

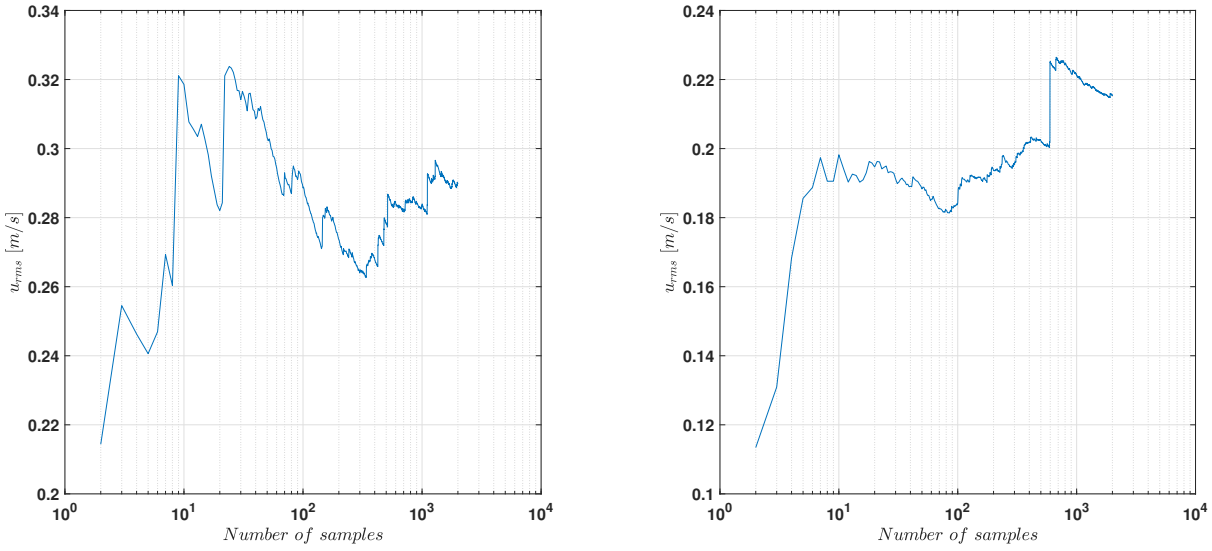

(a) Test case: Grid3

(b) Test case: Grid2

Figure 8: Convergence study on absolute value of u_{rms}. x-axis: number of samples used for the calculating the value of u_{rms} (in m/s). (a) and (b) show the results obtained for test case Grid3 and Grid2 respectively.

Figures 9a-9c show the auto-correlation function ($\rho_{11}(r, s = 0)$) of NO Grid case at three inlet velocities.

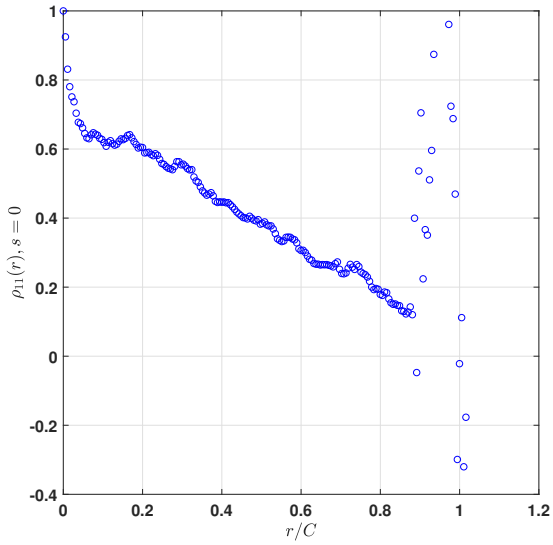

(a) Test case: U_{0set} =3m/s

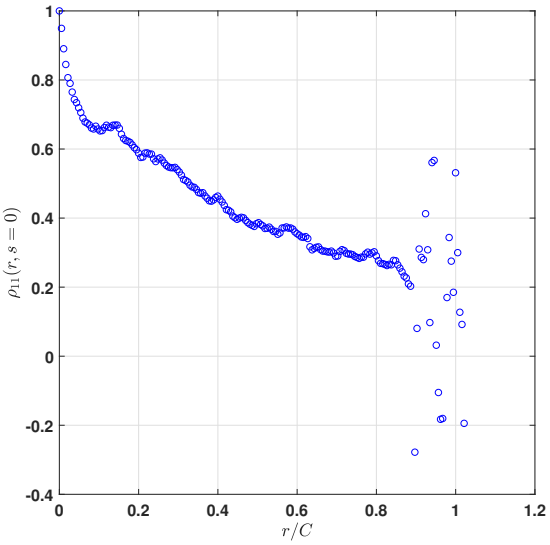

(b) Test case: U_{0set} =2m/s

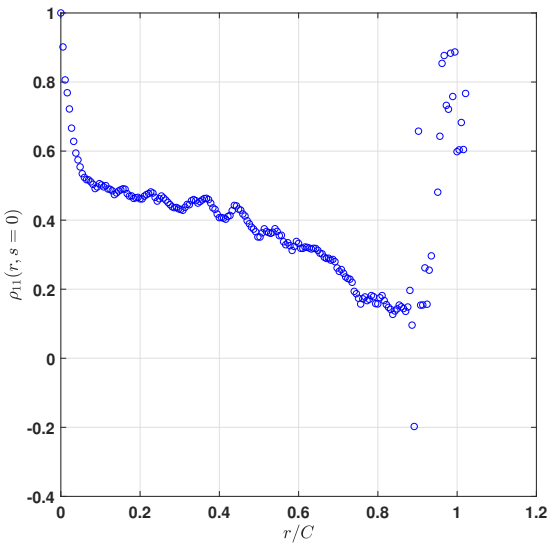

(c) Test case: U_{0set} =1m/s

Figure 9: Auto correlation coefficient for NoGrid cases.(a)-(c) show results for the different inlet velocities (U_{0set}).

Bibliography

[1] Spyros A Kinnas. An international consortium on high-speed propulsion. *Marine Technology and SNAME News*, 33(3):203, 1996.

[2] common.Wikimedia.org *Erosion of propeller*. https://commons.wikimedia.org/wiki/

[3] van Terwisga T.J.C. Cavitation on ship propellers, Chapter 9. *TU Delft OCW,https://ocw.tudelft.nl/courses/cavitation-ship-propellers/* 2016

[4] Jean-Pierre FRANC , LEGI (Grenoble, France) *Cavitating tip vortex*. http://www.legi.grenoble-inp.fr/

[5] Bosschers Johan *Propeller tip-vortex cavitation and its broadband noise*. PhD Thesis,UTwente, The Netherlands, 2018.

[6] Franc Jean-Pierre and Michel Jean-Marie *Fundamentals of cavitation*. Number 76. Springer science & Business media, 2006.

[7] Ronald J Adrian, and Jerry Westerweel. *Particle image velocimetry*. Number 30. Cambridge University Press, 2011.

[8] SCC Bailey and S Tavoularis. Measurements of the velocity field of a wing-tip vortex, wandering in grid turbulence. *Journal of Fluid Mechanics*, 601:281–315, 2008.

[9] Sean CC Bailey, Stavros Tavoularis, and Benedict HK Lee. Effects of free-stream turbulence on wing-tip vortex formation and near field. *Journal of Aircraft*, 43(5):1282–1291, 2006.

[10] Promode R Bandyopadhyay, Robert L Ash, and Daniel J Stead. Organized nature of a turbulent trailing vortex. *AIAA journal*, 29(10):1627–1633, 1991.

[11] George Keith Batchelor and AA Townsend. Decay of vorticity in isotropic turbulence. *Proceedings of the Royal Society of London. Series A. Mathematical and Physical Sciences*, 190(1023):534–550, 1947.

[12] George Keith Batchelor and Albert Alan Townsend. Decay of isotropic turbulence in the initial period. *Proceedings of the Royal Society of London. Series A. Mathematical and Physical Sciences*, 193(1035):539–558, 1948.

[13] GK Batchelor. Axial flow in trailing line vortices. *Journal of Fluid Mechanics*, 20(4): 645–658, 1964.

[14] ML Beninati and JS Marshall. An experimental study of the effect of free-stream turbulence on a trailing vortex. *Experiments in Fluids*, 38(2):244–257, 2005.

[15] WK Blake. Propeller cavitation noise: the problems of scaling and prediction. In *ASME Proc. Int. Symp. on Cavitation and Multiphase Flow Noise*, pages 89–100, 1986.

[16] JI Cardesa, TB Nickels, and JR Dawson. 2d piv measurements in the near field of grid turbulence using stitched fields from multiple cameras. *Experiments in fluids*, 52(6): 1611–1627, 2012.

[17] William K George. The decay of homogeneous isotropic turbulence. In *Proc. 2nd Int. Symp. on Transport Phenomena in Turbulent Flows. In: Transport phenomena in turbulent flows.(eds. Hirata, M*, pages 3–16, 1988.

[18] Hari C Ghimire and Sean CC Bailey. An experimental investigation of wing-tip vortex decay in turbulence. *Physics of Fluids*, 29(3):037108, 2017.

[19] Laurent Graftieaux, Marc Michard, and Nathalie Grosjean. Combining piv, pod and vortex identification algorithms for the study of unsteady turbulent swirling flows. *Measurement Science and technology*, 12(9):1422, 2001.

[20] Edward M Greitzer, Choon Sooi Tan, and Martin B Graf. *Internal flow: concepts and applications*, volume 3. Cambridge University Press, 2007.

[21] Frank Holzäpfel, Thomas Hofbauer, Denis Darracq, Henri Moet, François Garnier, and Cecile Ferreira Gago. Analysis of wake vortex decay mechanisms in the atmosphere. *Aerospace Science and Technology*, 7(4):263–275, 2003.

[22] T Hommes, J Bosschers, and HWM Hoeijmakers. Evaluation of the radial pressure distribution of vortex models and comparison with experimental data. In *Journal of Physics: Conference Series*, volume 656, page 012182. IOP Publishing, 2015.

[23] Thomas Kurian and Jens HM Fransson. Grid-generated turbulence revisited. *Fluid dynamics research*, 41(2):021403, 2009.

[24] P Lavoie, L Djenidi, and RA Antonia. Effects of initial conditions in decaying turbulence generated by passive grids. *Journal of Fluid Mechanics*, 585:395–420, 2007.

[25] Philippe Lavoie, Paolo Burattini, Lyazid Djenidi, and Robert A Antonia. Effect of initial conditions on decaying grid turbulence at low r λ. *Experiments in fluids*, 39(5):865–874, 2005.

[26] EM Laws and JL Livesey. Flow through screens. *Annual review of fluid mechanics*, 10 (1):247–266, 1978.

[27] Mohsen S Mohamed and John C LaRue. The decay power law in grid-generated turbulence. *Journal of Fluid Mechanics*, 219:195–214, 1990.

[28] Philippa L O'Neill, David Nicolaides, D Honnery, Julio Soria, et al. Autocorrelation functions and the determination of integral length with reference to experimental and numerical data. In *15th Australasian fluid mechanics conference*, volume 1, pages 1–4. Univ. of Sydney Sydney, NSW, Australia, 2004.

[29] P.C Pennings. *Dynamics of Vortex Cavitation*. PhD thesis, TU Delft, The Netherlands, 4 2016.

[30] PC Pennings, J Bosschers, J Westerweel, and TJC Van Terwisga. Dynamics of isolated vortex cavitation. *Journal of Fluid Mechanics*, 778:288–313, 2015.

[31] C Poelma, J Westerweel, and G Ooms. Turbulence statistics from optical whole-field measurements in particle-laden turbulence. *Experiments in Fluids*, 40(3):347–363, 2006.

[32] Stephen B. Pope. *Turbulent Flows*. Cambridge University Press, 2000. doi: 10.1017/CBO9780511840531.

[33] HJ Prins, MB Flikkema, J Bosschers, Y Koldenhof, CAF de Jong, C Pestelli, H Mumm, H Bretschneider, V Humphrey, and M Hyensjö. Suppression of underwater noise induced by cavitation: Sonic. *Transportation Research Procedia*, 14:2668–2677, 2016.

[34] EP Rood. Mechanisms of cavitation inception. *Journal of Fluids Engineering*, 113(2): 163–175, 1991.

[35] Philippe R Spalart. Airplane trailing vortices. *Annual Review of Fluid Mechanics*, 30 (1):107–138, 1998.

[36] G. I. Taylor. Statistical theory of turbulence. *Proceedings of the Royal Society of London. Series A, Mathematical and Physical Sciences*, 151(873):421–444, 1935. ISSN 00804630. URL `http://www.jstor.org/stable/96557`.

[37] Milton Van Dyke and Frank M White. An album of fluid motion, 1982.

[38] Tom van Terwisga, Erik van Wijngaarden, Johan Bosschers, and Gert Kuiper. Achievements and challenges in cavitation research on ship propellers. *International shipbuilding progress*, 54(2-3):165–187, 2007.

[39] Scott Veirs, Val Veirs, and Jason D Wood. Ship noise extends to frequencies used for echolocation by endangered killer whales. *PeerJ*, 4:e1657, 2016.

[40] Moore, Derek William and Saffman, Philip Geoffrey Axial flow in laminar trailing vortices. *Proceedings of the Royal Society of London. A. Mathematical and Physical Sciences*, 333:491–508, 1973.

[41] Fruman, DH and Cerrutti, P and Pichon, T and Dupont, P Effect of hydrofoil planform on tip vortex roll-up and cavitation. , 333:491–508, 1995.

[49] Melander, Mogens V and Hussain, Fazle Coupling between a coherent structure and fine-scale turbulence. *Physical Review E*, 333:48–4, 1992.

[43] Ghimire, Hari C and Bailey, Sean CC Experimental examination of vorticity stripping from a wing-tip vortex in free-stream turbulence. *Physical Review Fluids*, 113(3):3–3, 2018

[44] Bailey, Sean CC and Pentelow, Steffen and Ghimire, Hari C and Estejab, Bahareh and Green, Melissa A and Tavoularis, Stavros Experimental investigation of the scaling of vortex wandering in turbulent surroundings. *Journal of Fluid Mechanics,Cambridge University Press*, 843(3):722–747, 2018

[45] Van Jaarsveld, JPJ Holten, APC Elsenaar, A Trieling, RR and Van Heijst, GJF. An experimental study of the effect of external turbulence on the decay of a single vortex and a vortex pair. *Journal of Fluid Mechanics*, 670:(0) 214–239, 2011

[46] De Karman Theodore and Howarth Leslie On the statistical theory of isotropic turbulence. block *Proceedings of the Royal Society of London. Series A-Mathematical and Physical Sciences* ,164:(917) 192–215, 1938

[47] Liu HT Effects of ambient turbulence on the decay of a trailing vortex wake block *Journal of Aircraft* 29(2) 255–263, 1992

[48] Sarpkaya Turgut Decay of wake vortices of large aircraft. block *AIAA journal* 36(9) 1671–1679, 1998

[49] Melander Mogens V and Hussain Fazle Coupling between a coherent structure and fine-scale turbulence. block *Physical Review E* 48:(4) 2669–2669, 1993

[50] Tennekes Hendrik and Lumley JL and others A first course in turbulence. block *MIT press* , 1972

[51] Miyazaki Takeshi and Hunt Julian CR Linear and nonlinear interactions between a columnar vortex and external turbulence. *Journal of Fluid Mechanics,Cambridge University Press*, 402(3):349–378, 2000

[52] Wieneke B Stereo-PIV using self-calibration on particle images. *Experiments in fluids,Springer*, (39):267–280, 2005